Role of Water and Hydroxyl Groups in the Structures of Stetindite and Coffinite, MSiO4 (M = Ce, U)

Andrew C Strzelecki, Thomas Barral, Paul Estevenon, Adel Mesbah, Vitaliy Goncharov, Jason Baker, Jianming Bai, Nicolas Clavier, Stephanie Szenknect, Artaches Migdisov, et al.

Role of water and hydroxyl groups in the structures of stetindite and coffinite, $MSiO_4$ (M = Ce, U)

Andrew C. Strzelecki[1,2,3,†], **Thomas Barral**[1,2,4,†], Paul Estevenon[4,5], Adel Mesbah[4], Vitaliy Goncharov[1,2,3,6], Jason Baker[6], Jianming Bai[7], Nicolas Clavier[4], Stephanie Szenknect[4], Artaches Migdisov[6], Hongwu Xu[6], Rodney C. Ewing[8], Nicolas Dacheux[4], Xiaofeng Guo[1,2,3,*]

[1] *Department of Chemistry, Washington State University, Pullman, Washington 99164, United States*

[2] *Alexandra Navrotsky Institute for Experimental Thermodynamics, Washington State University, Pullman, Washington 99164, United States*

[3] *Materials Science and Engineering Program, Washington State University, Pullman, Washington 99164, United States*

[4] *ICSM, Univ Montpellier, CNRS, CEA, ENSCM, Site de Marcoule, Bagnols sur Cèze, 30207, France*

[5] *CEA, DES, ISEC, DMRC, Univ Montpellier, Site de Marcoule, 30207 France*

[6] *Earth and Environmental Sciences Division, Los Alamos National Laboratory, Los Alamos, New Mexico 87545, United States*

[7] *National Synchrotron Light Source II, Brookhaven National Laboratory, Upton, New York 11973, United States*

[8] *Department of Geological Sciences, Stanford University, Stanford, California 94305, United States*

[†] These two co-first authors have equal contribution.

* e-mail: x.guo@wsu.edu

Abstract: Orthosilicates adopt the zircon structure-types ($I4_1/amd$), consisting of isolated SiO_4 tetrahedra joined by A-site metal cations, such as Ce and U. They are of significant interest in the fields of geochemistry, mineralogy, nuclear waste form development and material science. Stetindite ($CeSiO_4$) and coffinite ($USiO_4$) can be formed under hydrothermal conditions despite both being thermodynamically metastable. Water has been hypothesized to play a significant role in stabilizing and forming these orthosilicate phases, though little experimental evidence exists. To understand the effects of hydration or hydroxylation on these orthosilicates, *in situ* high temperature synchrotron and laboratory-based X-ray diffraction was conducted from 25 °C to ~850 °C. Stetindite maintains its $I4_1/amd$ symmetry with increasing temperature but exhibits a discontinuous expansion along the *a*-axis during heating, presumably due to the removal of water confined in the [001] channels, which shrink against thermal expansion along the *a*-axis. Additional *in situ* high temperature Raman and FTIR spectroscopy also confirmed the presence of the confined water. Coffinite was also found to expand nonlinearly up to 600 °C, and then thermally decompose into a mixture of UO_2 and SiO_2. A combination of dehydration and dehydroxylation is proposed for explaining the thermal behavior of coffinite synthesized hydrothermally. Additionally, we investigated high temperature structures of two coffinite-thorite solid solutions, uranothorite ($U_xTh_{1-x}SiO_4$), which displayed complex variations in composition during heating that was attributed to the negative enthalpy of mixing. Lastly, for the first time, the coefficients of thermal expansion of $CeSiO_4$, $USiO_4$, $U_{0.46}Th_{0.54}SiO_4$, and $U_{0.9}Th_{0.1}SiO_4$ were determined to be $\alpha_V = 4.21 \times 10^{-6}$ °C^{-1}, 14.29×10^{-6} °C^{-1}, 17.21×10^{-6} °C^{-1}, and 17.23×10^{-6} °C^{-1}, respectively.

Keywords: Orthosilicate; high temperature structure; confined water; coefficients of thermal expansion (CTE), hydroxylation; thermal expansion; actinide geochemistry

TOC:

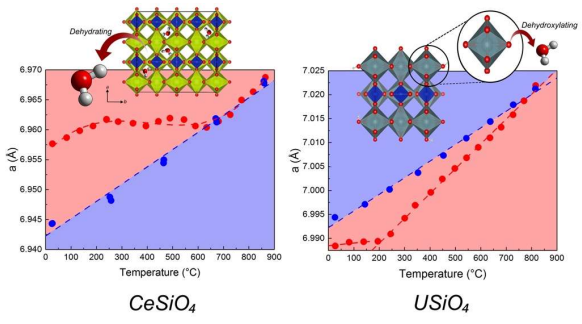

1. Introduction

The role of water is integral to both the thermodynamics and structures of many mineral systems and synthetic compounds.[1,2] In some systems the hydration and dehydration of the associated chemical components result in distinct minerals or phases, such as gypsum-anhydrite, polyhalite-anhydrite, studtite-metastudtite, and rhabdophane-monazite.[3–8] However, hydration and dehydration processes do not necessarily result in an obviously different atomic structure.[9–12] Subtle changes to the structure pose a challenge for correctly characterizing the state of water and its role during dehydration or mineral formation. Coffinite ($USiO_4$) is one of such mineral where the role of water is much debated.[13–16] Three different types of water can be associated with coffinite and other zircon structure-type phases: *i*) molecular water adsorbed onto the surface, *ii*) molecular water that is internally confined in the structure[12] (e.g., the [001] channel), and *iii*) structural water or hydroxyl substituting O^{2-} in the SiO_4^{4-} tetrahedra.[11,12] Previously, both Fourier transform infrared spectroscopy (FTIR) and powder X-ray diffraction (XRD) elucidated that water had no structural role in coffinite,[13,14,17–21] while Janeczek hypothesized that water may be confined in the structural channel.[21] Additionally, high temperature calorimetric studies suggested that water associated with coffinite included a fraction of water molecules that are adsorbed onto the mineral surface, and another portion more strongly bonded within the structure.[22] This plays an important role in the formation of coffinite, by lowering the overall enthalpy required for its natural formation. Likewise, uranothorite ($U_xTh_{1-x}SiO_4$) and stetindite ($CeSiO_4$), which are isostructural to coffinite ($I4_1/amd$, Figure 1), exhibit similar hydration dependencies that again were revealed by calorimetry.[23,24]

Investigations into the structural and thermodynamic properties of coffinite, uranothorite, and stetindite have also significant implications outside the fields of geochemistry and mineralogy, because these mineral phases are considered as potential ceramic waste forms for the immobilization of actinides.[25–30] Indeed, zircon ($ZrSiO_4$) has demonstrated advantages of extreme chemical and physical durability across geologic time,[31–36] implying considerable durability as an actinide host. While it has been shown that a zircon doped with 10 wt% ^{239}Pu would become fully amorphous after only 1,400 years,[37] preliminary calculation have shown that very little Pu would be ultimately released over a 500,000 year time span due to the relatively short half-life of ^{239}Pu as well as the retained low solubility of amorphous zircon.[25,27] Thus, as uranium is the main component of spent nuclear fuel[25,27,38–40] and cerium constitutes a useful surrogate for plutonium,[41–44] these minerals are also representative of how long-lived actinides will behave when incorporated into the zircon structure. These actinide-loaded crystalline waste forms would then be permanently disposed of in either a mined geologic repository or deep borehole.[32,45–47]

However, any potential immobilization matrix disposed of in either of the geologic disposal strategies will encounter elevated temperatures, ranged between 70 °C and 350 °C, as a result of the radiogenic decay heat mainly generated by short lived radionuclides.[48–52] Thus, a fundamental understanding of the thermal behavior of such solid solution is needed. Previous thermogravimetric analysis (TGA) coupled with differential scanning calorimetry (DSC) on stetindite performed by Strzelecki *et al.* (2020)[23] showed a sluggish dehydration from room temperature to 900 °C.[23] However, the structural information accompanying the dehydration process and beyond that dictates the measured mass and energetic events is largely lacking. Similarly, the calorimetric studies reported by Guo *et al.*[22] and Reynolds *et al.*[53] showed that there may be two water-bonded sites associated with coffinite. The first one is associated to rapid released water near 150 °C, while the more strongly bonding water was removed at temperatures ranging from 275 °C to ~600 °C. The first release is associated with weakly bonded water that was adsorbed onto the surface of the sample.[22,53] Conversely, the origin of the second release is still unclear, suggesting that some water is strongly interacting with the sample either as confined molecular water and/or attached hydroxyl groups (OH^-). Indeed, the zircon structure-type can have structurally incorporated water[13,54–56] and OH^-.[14,19,56,57] More recent studies discussed the mechanism of hydroxylation in the zircon structure and the impact from these groups on the material properties.[11,58–61] However, the exact proportion and origin of attached hydroxyl ions is debated; these include whether such incorporation is an indirect result of radiation-induced amorphization of natural zircon.[59,60,62] Nasdala *et al.*[62] proposed three crystallographic models for the location of hydroxyl groups in crystalline zircon: association with Si-vacant tetrahedrons, occupying SiO_4^{4-} tetrahedrons with or without a neighboring zirconium vacancy. Each of these cases can explain a different part of the results obtained by spectroscopy and thermal analysis in their study.[62] Interestingly, the nature of "embedded" water may have some impacts on the coffinite matrix, resulting in distinct thermal signatures and stabilities. Both natural and synthetic coffinite thermally degrades between 400 °C to 500 °C,[63,64] at which it undergoes a complete decomposition into amorphous SiO_2, UO_2 and U_3O_8 in air atmosphere.[22,65]

Here, we report the high temperature behaviors and structural parameters of a series of zircon structure-types with hydrothermal origins: stetindite, coffinite, and uranothorite solid solutions up to ~850 °C by performing *in situ* high temperature synchrotron and laboratory-based X-ray diffraction studies implementing with Rietveld analyses. During heating, all of these zircon structure-types exhibited temperature-dependent anisotropic thermal expansion behavior and discontinuous thermal expansion of the *a*-axis, from which we derived critical information about the "strongly bonded" water and its role in dehydration and hydration processes. For stetindite, the discontinuous expansion of the *a*-axis was interpreted to be confined molecular water along the [001] channel and offered an explanation to the "energetically strongly associated" water discussed by Strzelecki *et al.*[23]. Whereas for coffinite, the

discontinuous expansion of the *a*-axis during heating, in conjunction with a larger unit cell after cooling down, was attributed to a combination of dehydration and dehydroxylation, consistent with their "strongly bonded" features characterized by Guo *et al.*[22]. In addition, for the first time we report the coefficients of thermal expansion (CTEs) for each of these minerals.

2. Experimental Methods

2.1. Sample synthesis:

$CeSiO_4$ samples were synthesized by hydrothermal method from Ce(III)-silicate solid precursor (A-$Ce_2Si_2O_7$) according to the protocol described by Estevenon *et al.*[66]. A stoichiometric mixture of CeO_2 (Sigma Aldrich, particle size < 5 μm) and SiO_2 (Sigma Aldrich, 10-20 nm) was mechanically milled (30 Hz, 1 hour) in a Retsch MM 200 vibration mill mixer using a tungsten carbide milling vessel. This mixture was pelletized by uniaxial pressing under 5 MPa at room temperature and then heated at 1350 °C under reducing atmosphere (Ar–4% H_2) to prepare the Ce(III)-silicate solid precursor, A-$Ce_2Si_2O_7$ (space group: $P4_1$). 200 mg of A-$Ce_2Si_2O_7$ was then placed in contact with 4 mL of a 0.75 M HNO_3 solution (prepared by dilution of ACS grade 70% HNO_3, Sigma Aldrich). The pH of that solution was adjusted to 7.0 ± 0.1 with a freshly prepared NaOH solution (from ACS grade NaOH pellets, Sigma Aldrich). This mixture was then hydrothermally treated for 7 days at 150 °C under air atmosphere in 23 mL Teflon lined Parr autoclaves. The final product was separated from the aqueous solution by centrifugation, washed twice with deionized water and once with ethanol and then finally dried overnight at 60 °C.

Coffinite and uranothorite samples were prepared by the protocol developed by Mesbah et al.[67] through modification of the previous procedure proposed by Fuchs and Hoekstra.[63,64] The reagents of Na_2SiO_3, NaOH, $NaHCO_3$ were supplied by Sigma-Aldrich and were of analytical grade. The uranium (IV) chloride solution was prepared by following the methodology developed by Dacheux *et al.*,[68,69] which required dissolving U metal chips, obtained from Commission d'ETAblissement des Méthodes d'Analyses (CETAMA), CEA Marcoule, France, in 6M HCl. The thorium (IV) chloride solution was prepared by dissolving thorium nitrate pentahydrate in 6M HCl and performing several cycles of evaporation and dissolution in 4M HCl in order to remove all traces of nitrates in the solution.[70] The final concentrations of the uranium chloride and thorium chloride solutions were determined by ICP-AES. The syntheses were performed under inert atmosphere (argon). It consisted of first dissolving Na_2SiO_3 (0.81 g, 6.66 mmol) in water and then slowly adding the corresponding amounts of uranium and thorium, always keeping an excess of 10 mol % of silicate in order to ensure the complete complexation of the actinides. The pH of the mixture was adjusted to 11.3 ± 0.1 by dropwise adding 8M NaOH. The solutions were then buffered to a pH of 8.7 ± 0.1 through the addition of $NaHCO_3$. The resulting green gelatinous mixtures were then transferred into 23 mL Teflon lined Parr autoclaves and placed into an oven at 250 °C for 7 days. The final products were

separated by centrifugation and washed twice with deionized water and finally once with ethanol. The solids were then dried overnight in air at room temperature. As previously reported,[67] the synthesis led to the formation of a mixture of $Th_{1-x}U_xSiO_4$, $Th_{1-x}U_xO_2$, and amorphous SiO_2. Therefore, in order to obtain pure coffinite and uranothorite samples, the resulting powders were purified through the protocol reported by Clavier *et al.*[71]. With this aim, 100 mg of powdered samples were put in contact with 50 mL of 0.01 M HNO_3 for 3 - 5 days, followed by washing in deionized water, then remaining solid was placed in 50 mL of 0.01 M KOH solution for 3 - 5 days. The remaining coffinite or uranothorite samples were contacted again with deionized water then subsequently recovered by centrifugation. This sequence was repeated until the samples were fully purified.

2.2. *Vibrational Spectroscopies:*

Both stetindite and coffinite were characterized spectroscopically through a combination of Raman spectroscopy and Fourier transformed infrared spectroscopy (FTIR). The Raman spectra were recorded with a Horiba-Jobin Yvon Aramis device equipped with an edge filter and Nd:YAG laser (532 nm). The laser beam was focused on the sample with an Olympus BX 41 microscope with a X50LMP objective, with a spot area of 1 μm^2. Prior to the analysis, the apparatus was calibrated with a silicon wafer, using the first-order Si line at 520.7 cm^{-1}. *In situ* high temperature Raman spectroscopy was performed on the stetindite sample utilizing the same spectroscopic setup previously described but differed by that the sample was placed in a platinum crucible and inserted into a Linkam TS-1500 heating device. A heating rate of 10 °C/min was applied until reaching the desired temperature (100, 200, 300, 400, 600, 800 °C) with 5 minutes of idle time between reaching each temperature point and acquisition of the spectrum in order to ensure thermal equilibrium. A separate Raman spectrum for stetindite was collected at room temperature after calcinating at 1000°C. *In situ* high temperature Raman spectroscopy was not possible for coffinite or uranothorites as a result of the inability to have a controlled atmosphere over the sample during the *in situ* heating. The spectra for stetindite are presented as the average of five scans, while the reported spectrum for coffinite is average of four scans which was done in order to minimize the measurement error, both had an acquisition time of 10 s.

The FTIR spectra of both stetindite and coffinite were recorded with a PerkinElmer FTIR Spectrum 100 device, where powdered samples were directly deposited onto the surface of an ATR crystal without any prior preparation. Spectra of stetindite were recorded in the 300–4000 cm^{-1} range, with a resolution of 2 cm^{-1}, whereas the spectrum collected of coffinite was recorded in the 400-4000 cm^{-1} range, with a resolution of 4 cm^{-1}. In order to collect *ex situ* high-temperature FTIR spectra of stetindite, samples were heated prior to being analyzed to the desired temperature (100, 200, 300, 400, 600, 800, 1000 °C) overnight and analyzed the following day upon cooling back to room temperature.

2.3. In situ high temperature powder X-ray diffraction (HT-PXRD):

In situ HT-PXRD of coffinite and stetindite was conducted at the Sector 28-ID-2 (XPD) of the National Synchrotron Light Source-II (NSLS-II) at Brookhaven National Laboratory. The wavelength of the X-ray beam was 0.1949 Å. The X-ray beam is delivered by a sagittally focusing double Laue crystal monochromator. The beam size at sample is 0.60 mm (horizontal) × 0.20 mm (vertical). The 2D XRD images were recorded with a Perkin-Elmer XRD 1621 Digital Imaging Detector. Stetindite powder was put in a silica glass capillary with one side opened to the air, while coffinite powder was sealed in a double-walled silica-glass capillary filled with Ar gas. The capillary was then inserted into a custom-built, Kanthal coil-based furnace under standard atmosphere for heating and cooling. A K-type thermocouple was mounted near the center of the heating coil and was used to monitor and to control the temperature. The sample temperature was calibrated by measuring the CTE of a standard ceria powder at different temperature points, with a heating rate of 20 °C/min. Data were collected every 50 °C during heating from RT to 865 °C and every 200 °C during cooling. Approximately 3 minutes of idle time was used between reaching each temperature point and data collection in order to ensure thermal equilibrium. All collected two-dimensional images were calibrated, masked, and integrated through the use of Dioptas.[72] The obtained XRD patterns of stetindite and coffinite were analyzed through Rietveld method using General Structure Analysis System software version II (GSAS-II),[73] where the instrument parameters were obtained using a CeO_2 standard. The background was modelled by the Chebyshev function with 8 and 20 coefficients, respectively. The above Rietveld refinement procedures on HT-PXRD were also stated previously elsewhere.[7,74–77]

In situ HT-PXRD of two uranothorites (x = 0.46 and x = 0.90) were collected using a Bruker D8 advance diffractometer equipped with a Lynx-eye detector and using Cu $K\alpha_{1,2}$ radiation (λ = 1.54184 Å). PXRD patterns were collected by packing the powder in an alumina boat (0.8 mm of depth) which was placed inside an Anton-Paar high temperature chamber under a flow of He/H_2 (4%) to reduce the risk of the uranium oxidation. PXRD data were collected every 100 °C from room temperature to 1000 °C with a heating rate of 5 °C/min and a holding time of 15 mins before each measurement. Each PXRD pattern was collected for approximately one hour in the 2-theta range ($10° \leq 2\theta \leq 100°$). The obtained XRD patterns of the uranothorites were also analyzed via the Rietveld method but were performed using the Fullprof suite package.[78] Before the refinements, pure silicon was used to determine the instrumental function. The crystal structure was refined by allowing multiple parameters to vary such as the zero shift, unit cell parameters, isotropic atomic displacement, but the atomic coordinates were kept fixed because of the limited quality of our laboratory XRD data. Moreover, the microstructural effect was modelled using anisotropic size and strain functions in agreement with the Laue group of the zircon structure-type.

2.4 Sample Characterization:

The morphology of the samples was characterized by SEM with a FEI Quanta 200 Environmental Scanning Electron Microscope using backscattered electron detector (BSED) or secondary electron detector (SE) under vacuum conditions, at room temperature and with a low acceleration voltage of 3 kV for coffinite and 8 kV for stetindite in order to obtain high resolution images. The samples were always directly analyzed without any additional preparation step such as metallization. High-Temperature Environmental Scanning Electron Microscopy (HT-ESEM) experiments were performed using the same apparatus equipped with a HT1400 stage. The samples were heated with a 5 °C/min heating rate from room temperature to 600 °C and then with a 10 °C/min rate from 600 °C to 800 °C. The primary energy of the electron beam was 10 kV and the partial pressure in the ESEM chamber was 70 Pa. Images were recorded continuously during the experiment using the accumulation mode. More details are provided on Podor *et al.* (2019).[79] The results of which are supplied at the end of the SI. In addition, stetindite was previously characterized by extended X-ray absorption fine structure (EXAFS) and X-ray adsorption near edge structure (XANES)[66] for Ce oxidation state and local structures, and by thermogravimetric analysis coupled with differential scanning calorimetry (TGA-DSC) for its initial water content (0.43 mol H_2O per formula unit of $CeSiO_4$).[23]

3. Results

3.1 High-temperature synchrotron XRD of stetindite

The resulting refinements for stetindite yielded R_{wp} values ranging from 3.5% to 4.9% (Table S1). A representative fitted pattern of stetindite is shown in Figure 2. The refined unit cell parameters of stetindite are listed in Table S1 and gathered in Figure 3. The obtained U_{iso} values are listed in Table S1 and shown in Figure 4. The HT-PXRD patterns of stetindite (Figure S1) show its phase stability from RT to 865 °C under a standard air atmosphere. No phase transition or decomposition was observed during heating or cooling. It is in agreement with HT-ESEM observations for which no significant morphological changes were evidenced (Figures S10 to S23). However, phase transition may occur at higher temperatures. For instance, the isostructural mineral thorite ($ThSiO_4$)[13] undergoes a thorite ($I4_1/amd$) → huttonite ($P2_1/n$) transition above 1350 °C at 1 atm,[80–82] which has not been observed for stetindite. Although being thermally stable across the entire temperature range during heating, the high temperature behavior of stetindite can be separated into three regimes: *i*) 25 to 240 °C, *ii*) 240 to 634 °C, and *iii*) 634 to 865 °C. Such division is based on the non-linear expansion along the *a*-axis with temperature, where a plateau from 240 to 634 °C occurs between two linear-expansion regimes (Figure 3a). However, this discontinuity was much less pronounced along the *c*-axis, which exhibits a near linear thermal expansion (Figure 3b). Upon cooling stetindite from 865 °C to room temperature, the contractions along *a*- and *c*-axes both follow linear trends (Figure 3) as an extrapolation from that established in the third stage. The unit cell of stetindite upon

returning to room temperature after heating, has a smaller unit cell (a = 6.9443 Å and c = 6.1988 Å) compared to that of unit cell before heating (a = 6.9576Å and c = 6.2068) (Table S1).

3.2 High-temperature synchrotron XRD of coffinite

The resulting refinements for coffinite yielded R_{wp} values ranging from 3.3% to 9.3% (Tables S2). A representative fitted patterns for coffinite is shown in Figure 2. The refined unit cell parameters of coffinite are tabulated in Table S2 and presented in Figure 5. The associated U_{iso} values are tabulated in Table S2 and presented Figure 6. The HT-PXRD patterns of coffinite reveal a partial thermal decomposition starting at ~600 °C (Figures 7, 8, S2). A 10 mol % fraction of UO_2 identified at 816 °C (Table S3). This could be the result of two possible decomposition reactions: (1) $USiO_4 \rightarrow UO_2 + SiO_2$ in which the formed SiO_2 could remain amorphous and thus invisible from XRD[22,53,64,71,83–88] and/or (2) hydroxylated $USiO_4$ ($U(SiO_4)_{1-x}(OH)_{4x}\cdot nH_2O$) $\rightarrow$ anhydrous $USiO_4$ + UO_2.[11] These two reactions assume different coffinite starting types: the hydrated form, the hydroxylated form, or a combination of both, which will be discussed later. A plateau in the expansion of the unit cell was discovered along the a-axis and occurred over the temperature range of room temperature to ~200 °C. At higher temperatures (200 °C to ~450 °C) there was an almost linear unit cell expansion in the structure (5.2×10^{-5} Å/°C for parameter a). As coffinite was cooled, the contraction along the a-axis followed a linear trend but at a slower rate (4.96×10^{-5} Å/°C). Upon reaching room temperature, coffinite unit cell was slightly larger (a = 6.9944 Å and c = 6.2633 Å) than its original size (a = 6.9884 Å and c = 6.2668 Å) (Table S2).

3.3 High-temperature XRD of uranothorite, the solid solution

The refined unit cell parameters of each of the uranothorite solid solution are listed in Table S4 and reported in Figures S3 and S4. The high temperature behavior of uranothorite solid solution was similar to that observed for coffinite. There was a partial thermal decomposition of $U_xTh_{1-x}SiO_4$ (x = 0.46 and 0.90), leading to a mixture of UO_2, U_3O_8, and amorphous SiO_2 at ~800 °C (Figure S5). These results are in good agreement with the previous TGA-DSC studies that reported uranothorite to be thermally stable until 800 °C.[24] The presence of U_3O_8 as a decomposition product could be related to possible presence of air as an impurity in the measurement system or to the presence of traces of water in the helium atmosphere used for heating. The phase transition thorite ($I4_1/amd$) $\rightarrow$ huttonite ($P2_1/n$) was again excluded as it occurs at a higher temperature (1200-1225 °C).[82,89] A non-linear expansion of the unit cell was once again observed (Figures S3 and S4). For the higher U content (i.e., x = 0.9), the high temperature behavior is unique, showing a sharp decrease of the a parameter followed by a strong increase, coinciding with the opposite behavior of the c parameter (Figure S4). Such changes in the unit cell parameters may result from dynamically compositional changes of uranothorite at high temperatures. Uranothorite solid solution was found to have a negative enthalpy and volume of mixing.[24,90] $U_{0.9}Th_{0.1}SiO_4$, is close to coffinite which is

metastable, and it tends to decompose to a U-depleted uranothorite and surely led the excluded U that crystallized into U_3O_8, as driven by the energetic downhill towards thorite.[24] However, recent neutron diffraction data suggested a minimum unit cell parameter located around $x = 0.8$.[90] Thus, as the decomposed phase decreased from $x = 0.9$ to lower x values, the resulting unit cell was expected to decrease firstly till $x = 0.8$, then followed by a continuous increase when $x < 0.8$, in agreement with the above experimental results. On the other hand, $U_{0.46}Th_{0.54}SiO_4$, near the equal molar composition, has the maximum stabilization ($\Delta G = \Delta H - T\Delta S$) from the negative enthalpy of mixing[24] and the positive configurational entropic term of U and Th mixing.[90]

3.4 Vibrational spectroscopy of stetindite and coffinite

The $I4_1/amd$ space group has twelve active Raman vibrational modes, based upon that it belongs to the D_{4h} point group.[17,91,92] Of these twelve active modes, seven ($\Gamma_{int} = 2A_{1g} + 2B_{1g} + B_{2g} + 2E_g$)[91,92] can be assigned to the internal vibrations of the SiO_4 tetrahedron, while the remaining five ($\Gamma_{int} = 2B_{1g} + 3E_g$)[91,92] can be assigned to the external vibrations of the SiO_4 tetrahedrons within the unit cell.[91–93] Due to the interaction of the SiO_4 tetrahedrons with the MO_8 dodecahedrons in the unit cell, the SiO_4 tetrahedrons cannot be considered a strictly independent unit.[94] As a result of these interactions, there has yet to be a reporting of a spectra with all twelve of the active Raman modes for materials of the zircon structure-type.[17] Similar to what was found by Costin *et al.*,[17] only seven vibrational bands were presented for the stetindite (Figures 9a & 9b) and coffinite (Figure S6). Of the seven vibrational bands presented, four belong to the internal vibrational modes and occur near 420, 590, 900, and 920 cm^{-1}, while the three bands at 100, 200, 300 cm^{-1} are all due to the external vibrational modes. The positions of all the vibrational bands are in excellent agreement with previous Raman spectroscopic measurements on both compounds (Table S5).[17,66,95]

The *in situ* high temperature Raman spectroscopy of stetindite revealed that the sample studied in this study was compositionally pure and did not undergo any thermal decomposition, consistent with *in situ* high temperature XRD. This was confirmed as there were no observed vibrational peaks at 460 cm^{-1}, which would suggest the presence and/or the formation of CeO_2. The characteristic H_2O bending mode band around 1600 cm^{-1} and the OH stretching mode bands in the range 3500 – 3200 cm^{-1} are observed on the spectra collected at 200°C and 300°C (Figure 9c). However, the absence of the H_2O bending mode band for spectra obtained at room temperature and 100 °C is not explained yet and it is not possible to be sure these bands around 3500 – 2900 cm^{-1} correspond to water only or to both water and hydroxide bonds. This is consistent with the reports of Naslada *et al.* that Raman spectroscopy does often present problems in the detection of hydrous species in zircon structure-type due to their low intensity bands.[62] Lastly, there was a shift in the silicate bands located at 150 cm^{-1}, 280 cm^{-1} and 920 cm^{-1} for temperatures below 400 °C and a

disappearance of the bands located at 380 cm^{-1} and 510 cm^{-1} (which could correspond to M-OH bands) in the same temperature range (Figures S7 & S8).

For FTIR spectroscopy, the $I4_1/amd$ space group has seven active FTIR vibrational modes, which was determined again through a factor-group analysis.[17,91] Similar to Raman spectroscopy, these vibrational modes can be assigned to the internal and external vibrations of the SiO_4 tetrahedron. Of the seven vibrational modes, four ($\Gamma_{int} = 2A_{2u} + 2_{Eu}$) can be assigned to internal vibrational modes and three ($\Gamma_{ext} = A_{2u} + 2_{Eu}$) can be assigned to external vibrational modes. The four internal modes are presented for all of the calcinated stetindite samples (Figure 10) as well as the pristine coffinite sample (Figure S9). The four internal modes occur near 435, 570, 800, and 980 cm^{-1}. Again, the positions of all the vibrational bands are in excellent agreement with previous FTIR spectroscopic measurements on both compounds (Table S5).[17,66,95]

In contradiction to Raman spectroscopy, FTIR spectroscopy is often much more sensitive to vibrational modes of both H_2O and OH^-,[96] with the recorded FTIR spectra collected for the various calcinated stetindite samples and pristine coffinite sample demonstrating the following. For stetindite, a hydrous component was identified as two different bands. The first is a broad band between 3300-3400 cm^{-1} (Figure 10b), while the second is a broad and diffuse minor peak that is centered at 1635 cm^{-1} (Figure 10c). These bands can be attributed to the stretching and bending modes of H_2O, respectively.[11,62,96] Each of these two vibrational bands were found to disappear as temperature exceeded 400 °C (Figure 10).The FTIR spectra collected for the pristine coffinite sample displays a very broad and diffuse peak in the region from ~3700 to ~2950 cm^{-1} and also another broad and diffuse minor peak that is centered at 1636 cm^{-1} (Figure S10). Again, each of these peaks can be attributed to the stretching and bending modes of H_2O.[11,62,96] Interestingly, coffinite does display a peak centered 1088 cm^{-1} (Figure S9).[11,17] This vibrational band could indicate that coffinite is partially hydroxylated.

4. Discussion

4.1 Water in stetindite

The observed three-stage high temperature behavior of stetindite revealed by XRD (section 3.1) is in excellent agreement with the *in situ* high temperature Raman spectroscopy, the FTIR spectroscopy performed on the calcinated samples, and the previous TGA-DSC analysis by Strzelecki *et al.*[23] Indeed, these authors suggested that a portion of water was energetically more strongly associated with stetindite than that of surface adsorbed water as it was not fully removed until around 700 °C,[23] well corresponding to the first and second regimes (25 to 634 °C) shown by the XRD result (Figure 2a). The high temperature needed for removing this water also indicates the additional energetic contributions arise from the water-lattice interaction due to confinement that helps overcome the enthalpic penalty encountered by the

anhydrous phases.[23] The nature of this confined molecular water is further indicated by the Raman spectra where the presence and persistence of characteristic H_2O bending mode band around 1600 cm^{-1} and the OH^- stretching mode bands in the range 3500 – 3200 cm^{-1} up to 400 °C (Figure 9c). The temperature is obviously too high for physically adsorbed water to persist. FTIR further corroborates the existence of "strongly" associated water, as the bending and stretching vibrational bands of water did not disappear till temperatures exceeded 400 °C, as they were absent in the spectra collected for stetindite calcinated at above 600 °C (Figure 10).

Moreover, the removal of such confined water (accounts for approximately 87% of the water measured by TGA)[23], occurs between ~200 and ~700 °C, which is consistently overlapped with the second temperature regime (240 to 634 °C) in XRD where the *a*-axis undergoes a plateau, but the *c*-axis still follows a near linear expansion. This strongly suggests that removing of the confined water preferably impacts the lattice in the direction perpendicular to [001], causing the discontinuity in the expansion along the *a*-axis. Thus, we hypothesized that the confined water resides in the channels parallel to [001] (Figure 1b). Similar hypotheses have been proposed for other zircon structure-type phases,[13,14,55,56] including the one for coffinite by Janeczek in 1991.[21] Based on this hypothesis, the key structural feature of the confined water is its relative transitional freedom along the *c*-axis while being restrained in the (001) planes.[96,97] Hence, when thermal energy is provided to the confined water through heating, the thermal motion of the water molecules will gradually promote the breaking of the confinement and the release through the channels. As a result, the structure along the *a*-*b* planes is subject to the competition between the thermal expansion along the *a*-axis (or *b*-axis) and the contraction of [001] channels due to the void formation after water removal, which together leads to the plateau in the unit cell parameter *a* between 240 °C and 634 °C. While the structure along the *c*-axis receives a smaller impact from the breaking of confinement and thus follows a near linear expansion. This is further confirmed by measuring the bond distances constituting the channels size (Figure 11). As the channel is a parallelepiped, the three constituent bonds were selected to measure the height/width, diagonal, and the diagonal depth. The bonds which define the channels size are Ce (0, ¾, ⅞) – Ce (½, ¼, ⅝) or Si (0, ¾, ⅝) for the height/width; Ce (0, ¾, ⅞) – Si (½, ¾, ⅝) for the diagonal; and Ce (0, ¾, ⅞) – Ce (½, ¼, ⅜) for the depth. The variation for the size of the channels as a function of temperature (Figure 11) follows a nearly identical trend as observed for the *a*-axis (Figure 2a).

Further evidence supporting the dynamic interplay of confined water in the [001] channel comes from the investigation of the changes in the Si-O bond length and angle of the two sets of O-Si-O comprising the SiO_4 tetrahedron (Figure 12). This is shown by the fact that the Si-O (Si (1,0,0) – O (1,0,0)) bond distance contracts as a function of temperature (Figure 12a). The contraction begins at a gradual rate from room temperature to 394°C, followed by an acceleration in the contraction rate from 394 °C to 633 °C, reaching to a reduced Si-O bond length above 633°C. The longer Si-O bond length near ambient could be

a result of decreased electron density due to the formation of hydrogen bond with the same oxygen (Si-O-H) and hydrogen from the [001] confined water. Once the thermal energy was provided for the H_2O to be liberated from the channel, the Si-O bond can then relax and contract. The increase in the rate of contraction occurring over the temperature interval of 394°C to 633°C is again supported by the Raman and FTIR spectroscopic observations. Moreover, the shifts in the vibrational modes of SiO_4 bring additional information (Figures 9, S7, and S8). The vibrational frequencies of all the vibrational modes either plateau or decrease from room temperature to 200 °C. The symmetric internal stretching (ν_1) and the asymmetric stretching (ν_3) modes both increased to higher frequencies above 200°C (Figure S7b). While such a trend was not typically expected for high temperature Raman spectroscopy,[98] it was what has been found in high pressure Raman spectroscopy studies of zircon-type materials,[60,86,99] where the Si-O bond length decreased with increasing pressure, similar to the contraction of Si-O bond distance relating to ν_1 and ν_3 shifting to higher frequencies. The vibrational frequencies of the internal bending modes (ν_2 and ν_4) increased to higher frequencies from 200 °C to 600 °C, and then decreased to lower frequencies from 600 °C to 1000 °C (Figure S7a). As both the ν_2 and ν_4 vibrational modes were influenced by the vibrations of the Ce cation,[92] the behavior of these two modes was further complicated. The vibrational modes of all three external modes (Figure S8) were found to increase above 200 °C, again consistent with the decreased Si-O bond length.[60,86,99] The observed trend that vibrational frequencies either reached a plateau or decreased from room temperature to 200 °C may be due to the disappearance of the bands located at 380 cm^{-1} and 510 cm^{-1} which could correspond to M-OH bands. All of these shifts in both the internal and external vibrational bands (Figure S8 and S9) of the SiO_4 tetrahedron further support the elimination of water inserted in $CeSiO_4$ structure and the reorganization of the silicate structure. The changes in the angle of rotation of the two sets of O-Si-O, where set one is comprised of O (0,0,0) – Si (1,0,0) – O (1,0,0) and set two is comprised of O (1,1,1) – Si (1,0,0) – O (1,0,0), are to compensate the change in Si-O bond length (Figures 12b and 12c). This all further demonstrates that the hypothesized confined molecular water plays a major role in controlling the dynamics of the structural thermal expansion.

4.2 Hydroxyl group in coffinite

As it was previously mentioned in the result of *in situ* high temperature XRD of coffinite (section 3.2), the coffinite in this study was either of the hydrated form, the hydroxylated form, or a combination of both. This complexity of coffinite comes from its high temperature behavior which is different from that of stetindite in the following three points. First, the plateau in the expansion of the unit cell along the *a*-axis occurred in a much lower temperature range, from room temperature to ~200°C (Figure 5a), compared with stetindite. While the plateau corresponds well to water removal characterized by previous thermal analyses (TGA-DSC and mass spectrometry)[22,53] and the hypothesized water, which resides in the [001] channel, may explain the attenuation of thermal expansion, the relatively low temperature for removing the confined

water, suggests a weaker water-structure interaction. Second, the expansion of the unit cell at higher temperature (200 °C to ~450 °C) is almost linear (5.2×10^{-5} Å/°C for parameter *a*) (Figure 5c), as a result of the continued liberation of water and/or hydroxyl groups from coffinite as suggested by mass spectrometry.[22] This high-temperature structural behavior, different from that observed for stetindite, may be due to the presence of OH^- replacing O^{2-} in the SiO_4^{4-} tetrahedra.[11] As hydroxylated zircons exhibit a smaller unit cell size,[11] loss of OH^- groups would expand the structure. Such is further supported by the observation that at temperatures above 450 °C, the *a*-axis continued a near linear expansion at a rate of 5.2×10^{-5} Å/°C, as a result of mainly unit-cell thermal expansion and possible dehydroxylation. Third, the unit cell of coffinite after cooled to room temperature has a larger unit cell of 306.05(1) $Å^3$ compared to its original size, 306.41(2) $Å^3$ (Figure 5c and Table S2), supporting that the starting coffinite was hydroxylated with a smaller unit cell.

The hydroxylation is further supported by the following analysis of Si-O bond length and bond angle (Figure 13). The variance of Si-O bond length as a function of temperature was plotted in Figure 13a. From room temperature to 301°C, Si-O underwent a slight contraction, probably due to the removal of confined water similar to the Si-O contraction in stetindite (Figure 12). Then Si-O expanded from 301°C to 544°C, nearly coincident with the secondary mass loss observed by the previous TGA-DSC-MS studies.[22,53] Again, the changes in the angle of rotation of the two sets of O-Si-O are to compensate the change in Si-O bond lengths (Figure 13b & 13c). The overall observed trend of lengthening of Si-O bond length further indicates that the sample was mostly hydroxylated, again in agreement with hydroxylated zircons having a smaller unit cell due to the shorter Si-OH bond length.[11]

Thus, coffinite in this study is likely to be both partially hydrated and hydroxylated: $U(SiO_4)_{1-x}(OH)_{4x}\cdot nH_2O$, which is also supported by FTIR analysis, where both water stretching (~3700 to ~2950 cm^{-1}) and bending (1636 cm^{-1}) modes and OH^- stretching mode (1088 cm^{-1}) were identified (Figure S10).[11,17,62,97] Coffinite after dehydration and dehydroxylation was "cleaner", exhibiting a slightly larger size after heating, which is consistent with Caruba et al.[11] reporting an increase in unit-cell volume for hydroxylated zircons after heating to 950 °C. The above observation agrees well with previous reports on synthetic and natural coffinites. The average unit-cell values in the literature for synthetic (pristine and thermally treated) coffinite are ($\bar{a}$ = 6.989 Å and $\bar{c}$ = 6.266 Å, Table 1)[22,53,54,60,64,65,83–86] are in general larger than those for natural coffinites ($\bar{a}$ = 6.951 Å and $\bar{c}$ = 6.263 Å, Table 1).[57,64,100,101] Additionally, the complicated interplay between hydration and hydroxylation explains the discrepancy in the reported unit cell parameters for coffinite (Table 1).[22,52, 53,56,62–64,82–85,88,89] Finally, the differences in vibrational band and thermal behavior also indicate that hydrothermally prepared zircon structure-type phases could deviate from one another. Thus, $U(SiO_4)_{1-x}(OH)_{4x}\cdot nH_2O$ is probable and should commonly represent the phases encountered in nature or prepared via hydrothermal synthesis routes. As the hydroxylated coffinite can be

preserved in low temperature at which both synthetic and natural coffinites form, what we learnt from coffinite in this study should closely reflect its alteration at elevated temperature in nature. These above discoveries could be generalized towards other zircon structure-types (e.g., thorite, hafnon ($HfSiO_4$)) that have hydrothermal origins.[23,80,102,103]

4.3 Thermal response of metal orthosilicates

The mismatch in the *a* parameter before and after heating appears to be a unique feature of the synthetic stetindite and coffinite prepared by hydrothermal routes, which could be more generalized for other zircon structure-types with hydrothermal origins.[80,102,103] Metal orthosilicates synthesized from the dry routes, the usual method for preparing zircon, hafnon ($HfSiO_4$), and thorite, do not show such a sluggish thermal response, suggesting the absence of confined water or structural OH^-. Noted that the high temperature solid state routes[54,104–108] are possible for zircon, hafnon, and thorite (but not for coffinite, stetindite) because they all have energetically favorable enthalpy of formation ($\Delta H_{f,\,ox}$) from binary oxides ($MO_2 + SiO_2$).[24,104] In contrast, stetindite and coffinite are both energetically metastable with respect to their binary oxides and thus require hydrothermal synthetic techniques to obtain the pure phases,[22,23,66,95] in which water and/or OH^- play significant roles in stabilizing the formed silicates. Thus, although all of these zircon-type materials crystallize in the same long-range structure, the hydration and hydroxylation introduced during their formation can greatly modify their material signatures, high temperature behaviors, and thermodynamic properties.[22–24] This conclusion can be generalized to other natural metastable minerals having hydrothermal origins, such as the dichotomy pairs of monazite-rhabdophane or xenotime-churchite.[3,9,109,110]

For this reason, in order to compare high temperature structural data of stetindite and coffinite with other metal orthosilicates, such as zircon, hafnon, and thorite reported in studies of Mursic et al.[111], Ding et al.[112] and Knyazev et al.[89] (Table 2),[89,111–115] we used the XRD data obtained during cooling where samples were fully dehydrated or dehydroxylated. In addition, we normalized all the data by taking the relative change in unit cell parameters (a/a_0 and c/c_0) as a function of temperature (Figure 14). This shows that both stetindite and coffinite followed a similar thermal response of the *c*-axis in zircon, hafnon, and thorite. However, when observing the thermal response of the *a*-axis, stetindite and coffinite deviate slightly (by ~0.1%) from the group.

4.4 Coefficients of thermal expansion

As it is evident from the previous section that the hydrous and anhydrous forms expanded differently in response to thermal energy. Here we present two sets of coefficients of thermal expansion (CTEs) for the two forms. The mean CTEs for hydrous stetindite and hydroxylated coffinite are presented in SI. Note that the CTEs of hydrated phases are strongly dependent of the nature of the starting material

and susceptible to the synthesis conditions, therefore the CTEs of hydrated phases may not be representative.

The CTEs for anhydrous phases are considered as the standard values. Stetindite was found to be fully dehydrated above 634 °C. The following linear relations of unit-cell parameters for anhydrous stetindite were then derived by fitting the data obtained during the heating from 634 °C to 865 °C and the full cooling data from 860 °C to 25 °C ($R^2 > 0.987$):

$$a\ (\text{Å}) = 6.9421 + 2.9244 \times 10^{-5}\ T\ (°\text{C})$$
$$c\ (\text{Å}) = 6.1967 + 3.6518 \times 10^{-5}\ T\ (°\text{C})$$
$$V\ (\text{Å}^3) = 298.63 + 4.33 \times 10^{-3}\ T\ (°\text{C})$$

The derived mean CTEs of anhydrous stetindite are α_a(stetindite-anhyd) = 4.21 × 10^{-6} °C^{-1}, α_c(stetindite-anhyd) = 5.89 × 10^{-6} °C^{-1}, and α_V(stetindite-anhyd) = 14.49 × 10^{-6} °C^{-1}.

For dehydroxylated coffinite, only the unit-cell parameters during cooling from 815 °C to 31 °C were used to fit the CTEs to linear relations ($R^2 > 0.986$):

$$a\ (\text{Å}) = 6.9923 + 3.4732 \times 10^{-5}\ T\ (°\text{C})$$
$$c\ (\text{Å}) = 6.2613 + 2.7283 \times 10^{-5}\ T\ (°\text{C})$$
$$V\ (\text{Å}^3) = 306.12 + 4.39 \times 10^{-3}\ T\ (°\text{C})$$

The derived mean CTEs of dehydroxylated coffinite are α_a(coffinite-dehyd) = 4.96 × 10^{-6} °C^{-1}, α_c(coffinite-dehyd) = 4.35 × 10^{-6} °C^{-1}, and α_V(coffinite-dehyd) = 14.29 × 10^{-6} °C^{-1}. Previously, α_V(coffinite) has been calculated via density functional theory by Fleche[116] to be 17.0 × 10^{-6} °C^{-1}, disagreeing with our experimental value by 19%. Coffinite exhibited anisotropic expansion, with the *a*-axis expanding at a rate 1.14 times faster than that of *c*-axis. However, the inverse anisotropic expansion was found in stetindite, thorite, hafnon, zircon, and both compositions of uranothorite investigated in this study, with all the materials exhibiting a faster expanding rate along the *c*-axis (Table 2).[89,111–115] The anisotropic behavior can be explained from the perspective of arrangement of TO_4 tetrahedra and MO_8 dodecahedra, which can be also depicted as two intersected disphenoidal MO_4 forms: edge-sharing $MO1_4$ alternating with TO_4 along the *c*-axis, and $MO2_4$ corner sharing with another $MO2_4$ tetrahedra forming a zigzagging chain along the *a*-axis (Figure 1).[13,55,90] Thus, the zircon structure is more flexible along the *a*-axis due to the higher freedom of corner-sharing $MO2_4$ tetrahedra and can relax the structure during expansion, which results in a smaller change along the *a*-axis compared to the *c*-axis, along which the TO_4 is more incompressible.[90,117] Consequently, due to the higher repulsion experienced due to the edge sharing over corner sharing, the *c*-axis expands at a faster rate than that of the *a*-axis.

However, coffinite exhibits inverse anisotropic expansions (Figures 14 and 15, Table S6), when compared to other zircon-type orthosilicate phases. One possible cause for the inverse anisotropic expansion with a greater change of α_a is the unique bonding feature of U^{4+} in the eight-coordination

environment, which allows for more orbital overlap between U 5*f* and O 2*p* orbitals to form hybridization,[90,118–121] thereby contributing to partial covalent characters[90,121] particularly along the *a*-*b* planes.[90] Covalent bond is easier to be compressed or stretched than ionic bond, thus having larger variance in bond length of <U-O2> and size of $UO2_4$ tetrahedra during thermal expansion. Such expansion in addition to the unit cell expansion leads to a larger change in α_a than α_c. This explanation is also applicable to uranothorite though its chemistry is more complicated because of the internal polyhedral distortion due to the mixing of U and Th.[90] After all, all other potential reasons (vacancies, local ordering or oxidation of U^{4+} to U^{6+}) can only lead to the decrease in the expected α_a or affect only the uranothorite solid solutions.

Many thermodynamic variables of isostructural inorganic materials are able to be studied through the existence of different empirically derived relationships.[122–131] These empirically derived relationships link the specific thermodynamic variables to the varying component of the isostructural materials and allow to study the periodicity of said variable. Subbarao *et al.*[114] found one such way to study CTEs of zircon-type phases was by plotting the CTEs for several zircon structural materials versus the sum of the atomic weights of the A Site and B site cations. We employed such a methodology (Figure 15) [89,111–115] to explore the uniqueness of coffinite. Subbarao *et al*.[114] reported that CTEs of $M^{4+}T^{4+}O_4$ zircon-type phases decrease with increasing the overall mass of the A and B site cations. When viewing Figure 15 it can be seen that coffinite has α_a severely deviate from the trend in Figure 15a, [89,111–115] but α_c and α_V complies with trend in Figure 15b and Figure 15c, [89,111–115] respectively. As a result, the anisotropic behavior of coffinite also shows a large deviation from other zircon structure-type compositions (Figure 15d) [89,111–115]. Uranothorite solid solution deviates from all of these trends, as both compositions consistently have a higher CTE than would be expected for the corresponding A + B site mass.

5. Conclusions

The thermal behaviors of stetindite and coffinite were investigated by *in situ* high temperature synchrotron powder XRD, *in situ* high temperature Raman spectroscopy, and *ex situ* high temperature FTIR spectroscopy (on calcined samples) up to 900 °C. Stetindite was found to maintain its $I4_1/amd$ symmetry across the entire temperature gradient investigated. Coffinite, however, thermally decomposed to a mixture of UO_2 and SiO_2 at 600 °C. We also identified hydrous stetindite and hydroxylated coffinite, both of which showed non-linear expansions along the *a*-axis with increasing temperature. The removal of molecular water from the [001] channels in the zircon structure-type explained the discontinuous thermal expansion of hydrous stetindite. A combination of dehydration and dehydroxylation was proposed for synthetic coffinite, which exhibited a similar, yet less dramatic thermal expansion. Additionally, uranothorite had a similar high temperature behavior to that of coffinite, with a notable difference in thermal stability, controlled by the interplay of its negative enthalpy of mixing and volume of mixing. Lastly, the CTEs of

$CeSiO_4$, $USiO_4$, $(U_{0.9}Th_{0.1})SiO_4$, and $(U_{0.46}Th_{0.54})SiO_4$ were determined for the first time. Interestingly, $USiO_4$ showed a different anisotropic expansion than other zircon structure-types in that the *a*-axis expanded at a faster rate than the *c*-axis. Such an inverse in anisotropic expansion may be due to the directionality of partial covalent characteristics along the *a*-*b* planes as a result of U 5*f* – O 2*p* hybridization in the UO_8 dodecahedra.

Acknowledgements

This work was supported by the institutional funds from the Department of Chemistry at Washington State University. We also acknowledge the support by the U.S. Department of Energy, Office of Nuclear Energy, grant DE-NE0008582, the fund support from the Alexandra Navrotsky Institute for Experimental Thermodynamics, and the WSU-PNNL Nuclear Science and Technology Institute. Portions of this research were also supported by collaboration, services, and infrastructure through the Nuclear Science Center User Facility at WSU. Research presented in this article was supported by the Laboratory Directed Research and Development (LDRD) program of Los Alamos National Laboratory (LANL) under project number 20180007 DR. LANL, an affirmative action/equal opportunity employer, is managed by Triad National Security, LLC, for the National Nuclear Security Administration of the U.S. Department of Energy under contract 89233218CNA000001. This research used Beamline 28-ID-2 (XPD) of the National Synchrotron Light Source II, a U.S. Department of Energy (DOE) Office of Science User Facility operated for the DOE Office of Science by Brookhaven National Laboratory under Contract No. DE-SC0012704. The authors also thank Renaud Podor (ICSM) for supporting SEM and HT-ESEM experiments.

Tables

Table 1. Unit-cell parameters of synthetic coffinite compared to those published for synthetic and natural coffinite.

Reference	Publication date	*a* (Å)	*c* (Å)
Hoekstra and Fuchs[63]	1956	6.977	6.307
Fuchs and Gebert[53]	1958	6.981(4)	6.250(5)
Guo et al.[22]	2015	6.983(3)	6.263(4)
Labs et al. [83]	2014	6.9842(3)	6.2606(3)
Szenknect et al. [84]	2016	6.9856(2)	6.2582(2)
Mulak[85]	1977	6.986(2)	6.268(2)
Bauer et al. [86]	2014	6.9862(2)	6.2610(4)
Pristine coffinite (this study)	**2021**	**6.9884(1)**	**6.2668(1)**
Coffinite after heating (this study)	**2021**	**6.9944(2)**	**6.2633(3)**
Guo et al. [22]	2015	6.990(1)	6.261(1)
Zhang et al. [60]	2009	6.9936(4)	6.2614(6)
Reynolds[52]	2013	6.9980(2)	6.2720(2)
Pointeau et al. [65]	2009	7.0135(4)	6.2669(6)
Average values $\bar{a}$ and $\bar{c}$ (Å)	-	6.989	6.266
Stieff et al. [57]	1956	6.94	6.31
Hansley and Fitzpatrick[89]	1989	6.946(1)	6.268(2)
Darnley et al. [90]	1965	6.95(2)	6.26(3)
Darnley et al. [90]	1965	6.98(2)	6.19(3)
Hoekstra and Fuchs[63]	1956	6.937	6.285
Average values $\bar{a}$ and $\bar{c}$ (Å)	-	6.951	6.263

[*] The data above and below the dotted line are associated to synthetic and natural coffinite, respectively.

Table 2. Thermal expansion coefficients of orthosilicate compounds crystallizing in the zircon structure.

Compound	α_a ($\times 10^{-6}$/°C)	α_c ($\times 10^{-6}$/°C)	α_c/α_a	T range (°C)	Reference
$ZrSiO_4$	3.05	6	1.97	31-885	Mursic[111]
$ZrSiO_4$	3.2	5.4	1.69	20-520	Bayer[113]
$ZrSiO_4$	3.4	5.6	1.65	20-1020	
$ZrSiO_4$	3.5	6	1.71	20-800	Subbarao[114]
$ZrSiO_4$	3.8	6.5	1.71	25-1000	
$ZrSiO_4$	4.3	6.5	1.51	25-1500	
$ZrSiO_4$	3.9	6	1.54	25-500	
$HfSiO_4$	3.0	4.9	1.63	20-520	Bayer[113]
$HfSiO_4$	3.1	5.1	1.65	20-1020	
$HfSiO_4$	2.77	6.09	2.20	25-1200	Ding[112]
$HfSiO_4$	3.11	5.97	1.92	100-1250	
$HfSiO_4$	3.2	6.1	1.91	25-800	Varghese[115]
$CeSiO_4$ anhydrous	**4.21**	**5.89**	**1.40**	**25-885**	**This study**
$USiO_4$ dehydroxylated	**4.96**	**4.35**	**0.88**	**31-815**	**This study**
$(U_{0.46}Th_{0.54})SiO_4$	**4.65**	**7.93**	**1.71**	**400-800**	**This study**
$(U_{0.9}Th_{0.1})SiO_4$	**4.71**	**7.81**	**1.66**	**200-600**	**This study**
$ThSiO_4$	2.5	5.3	2.12	25-500	Subbarao[114]
$ThSiO_4$	3.5	5.1	1.46	25-900	Knyazev[89]

Figures

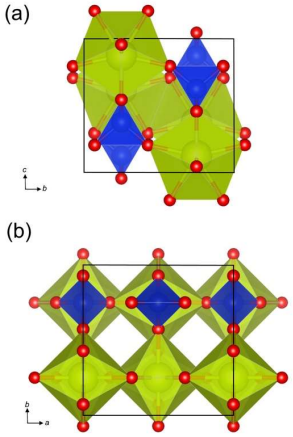

Figure 1. Projections of the structure of stetindite down to various crystallographic axes (prepared using the VESTA 3 software package[132]). In both **a** and **b** the *yellow dodecahedra* are the CeO_8, the *blue tetrahedra* are the SiO_4, and the *red spheres* are oxygen. **(a)** representation of the structure along [100]. **(b)** illustration of the structure along [001] showing clearly the channels where water may reside.

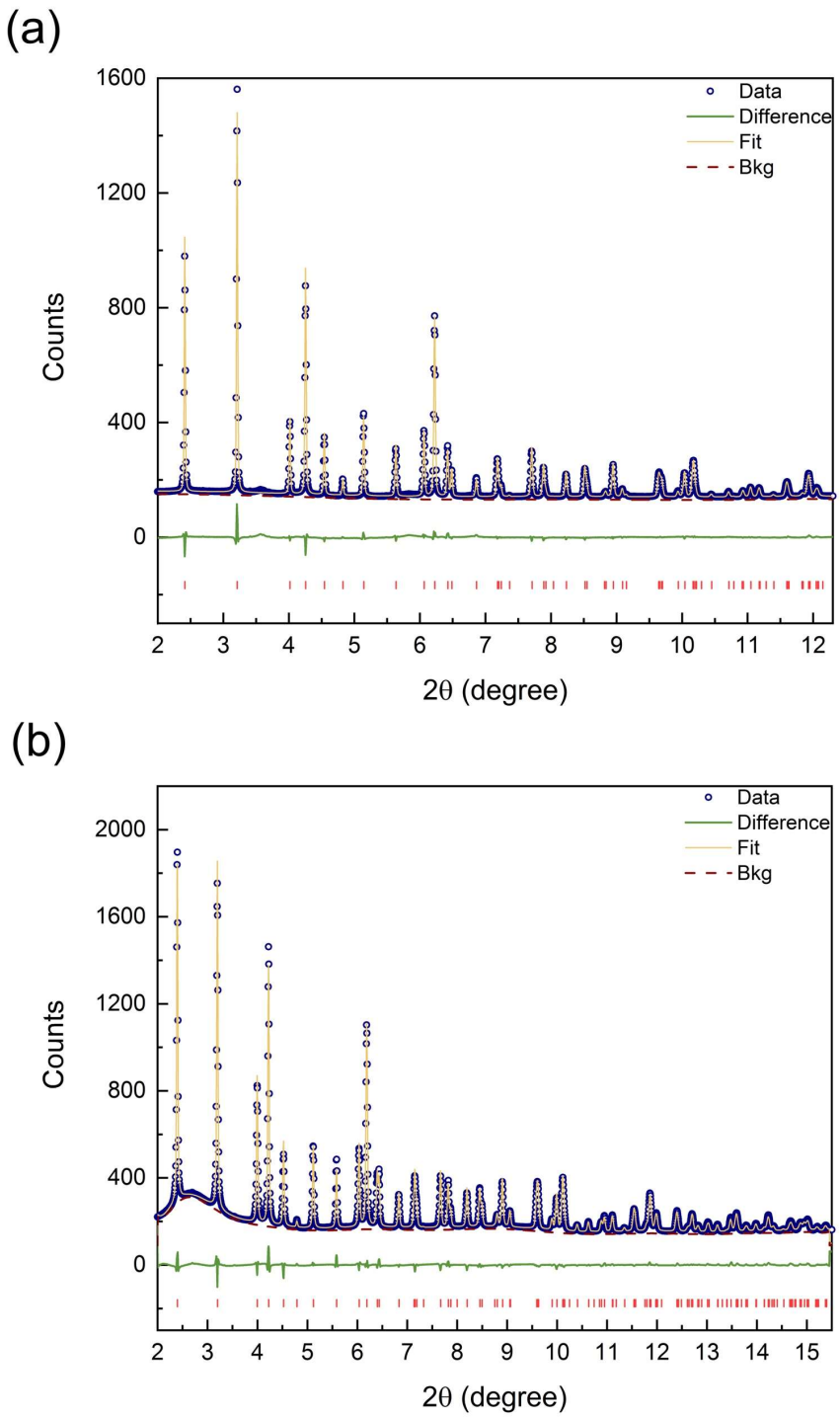

Figure 2. Fitted synchrotron XRD patterns of **(a)** stetindite at 27°C and **(b)** coffinite at 31°C. Data are shown as *open blue circles*, and the *solid yellow curve* is the best fit to the data. The *solid green* curve represents the difference between the observed and calculated profiles. The *red tick marks* above the *x*-axis indicate the positions of diffraction maxima.

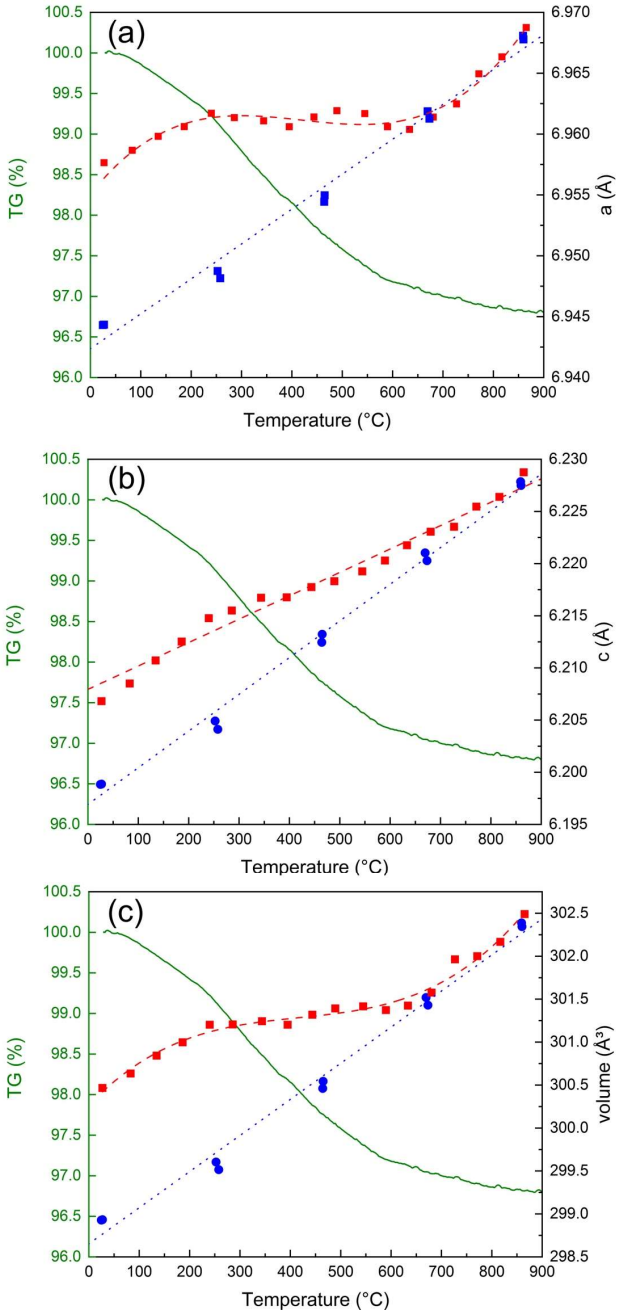

Figure 3. Variation of unit cell parameters for stetindite. *Red symbols* in both **(a), (b)** and **(c)** indicate the data points taken while heating the sample, and *blue symbols* indicate data points collected while cooling the sample. The exhibited TG data in *green curve* were published previously.[23]

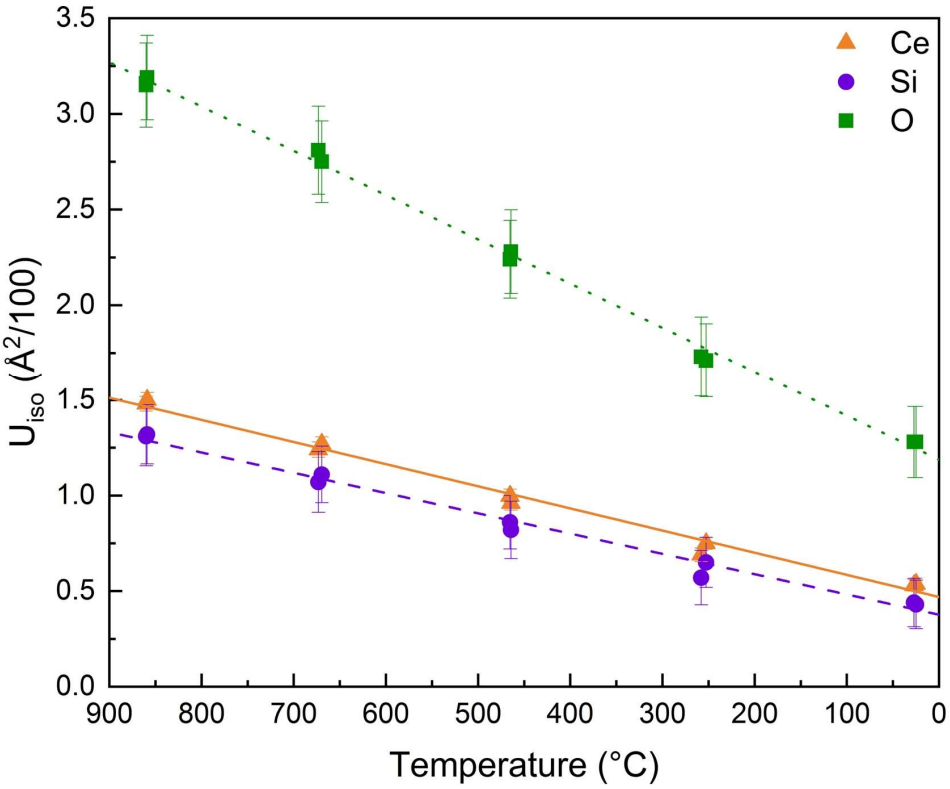

Figure 4. Variation of atomic thermal parameters of stetindite as a function of temperature. *Triangles* and *solid lines* represent Ce, *circles* and *dashed lines* represent Si, and *squares* and *dotted lines* represent oxygen.

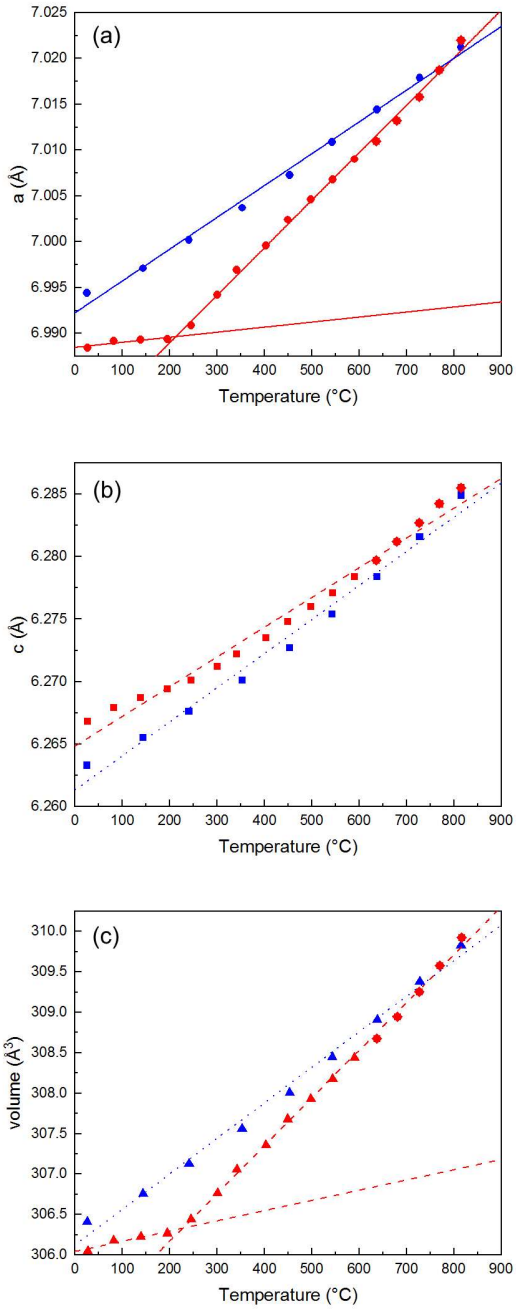

Figure 5. Variation of unit cell parameters for coffinite. Red symbols in both **(a), (b)** and **(c)** indicate the data points taken while heating the sample, while blue symbols indicate data points collected while cooling the sample. Red star symbols indicate measurements where $USiO_4$ observed to be decomposing to UO_2 starting at 636°C.

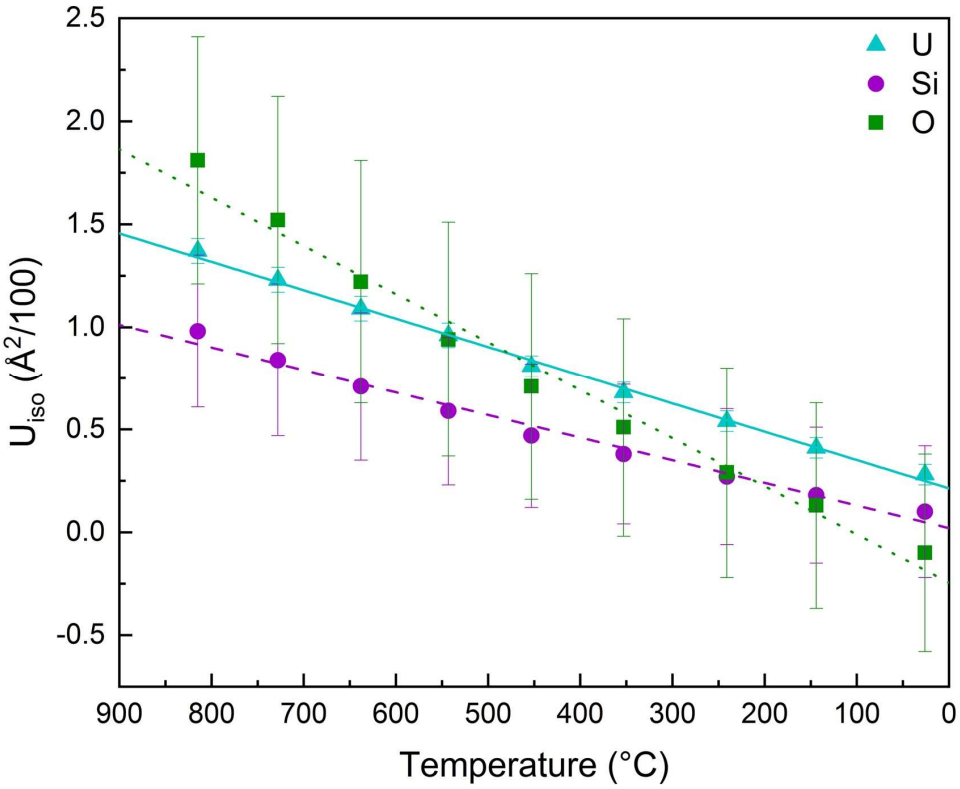

Figure 6. Variation of atomic thermal parameters of coffinite as a function of temperature. *Triangles* and *solid lines* represent U, *circles* and *dashed lines* represent Si, and *squares* and *dotted lines* represent O.

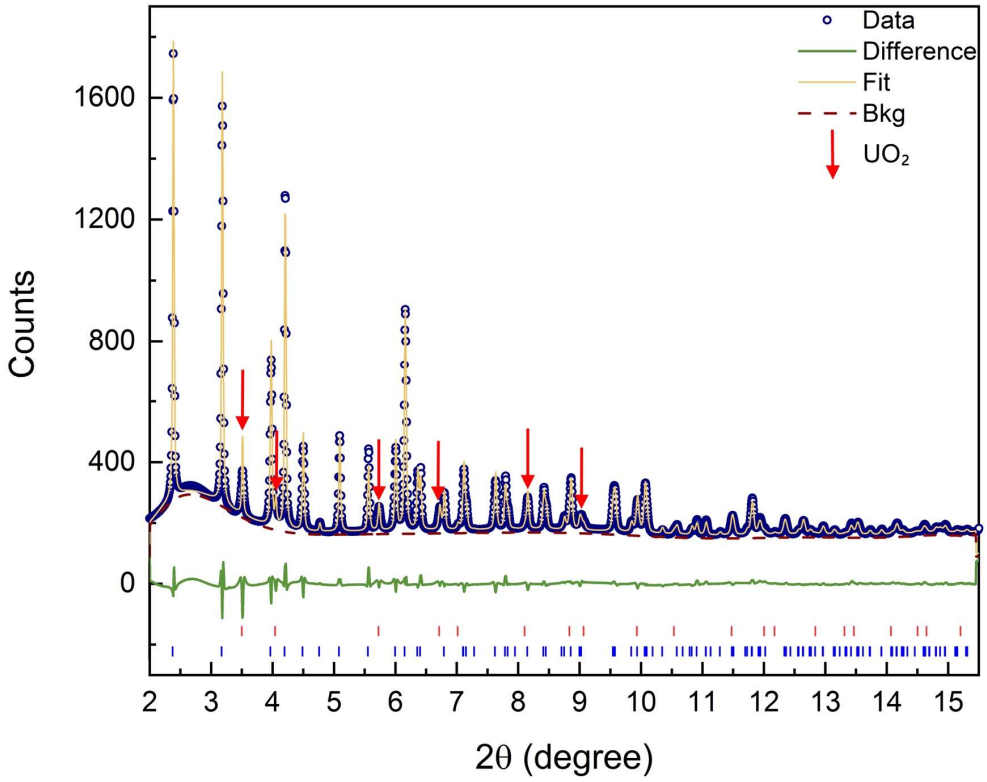

Figure 7. Fitted synchrotron XRD pattern of coffinite at 816 °C. Data are shown as *open blue circles*. *The solid yellow curve* is the best fit to the data. The *solid green* curve represents the difference between the observed and calculated profiles. The *blue tick marks* above the *x*-axis indicate the positions of allowed reflections for coffinite and the *red tick marks* indicate those for UO_2.

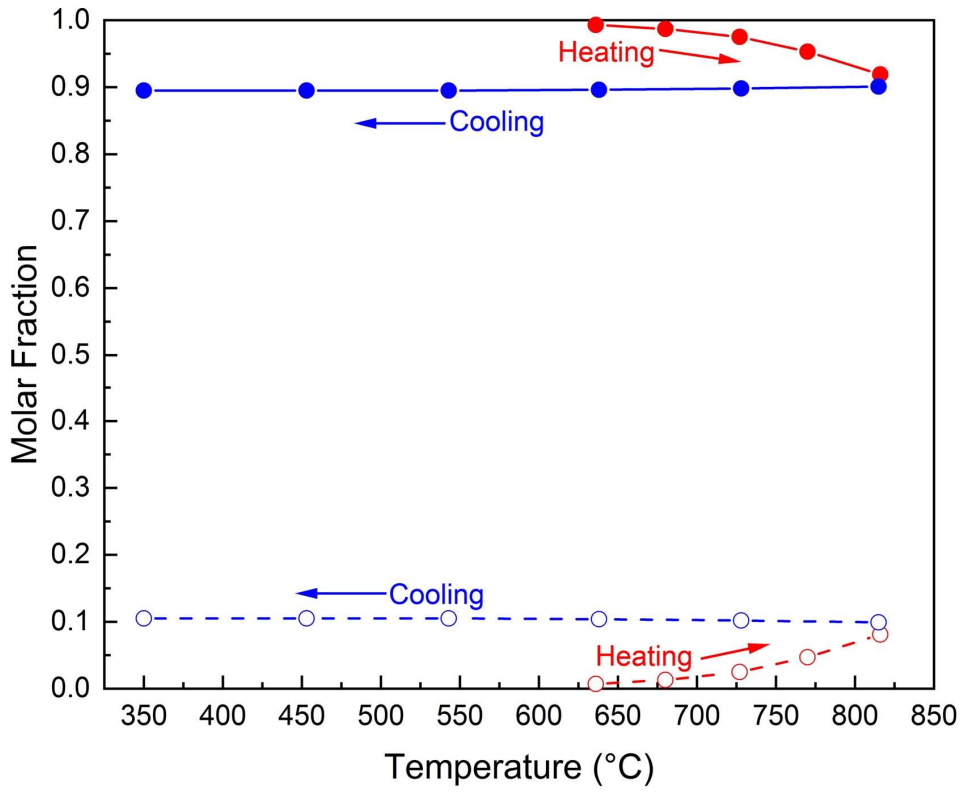

Figure 8. Variation of molar fraction of $USiO_4$ (*solid circles*) and UO_2 (*open circles*) upon heating (*red*) and then cooling (*blue*).

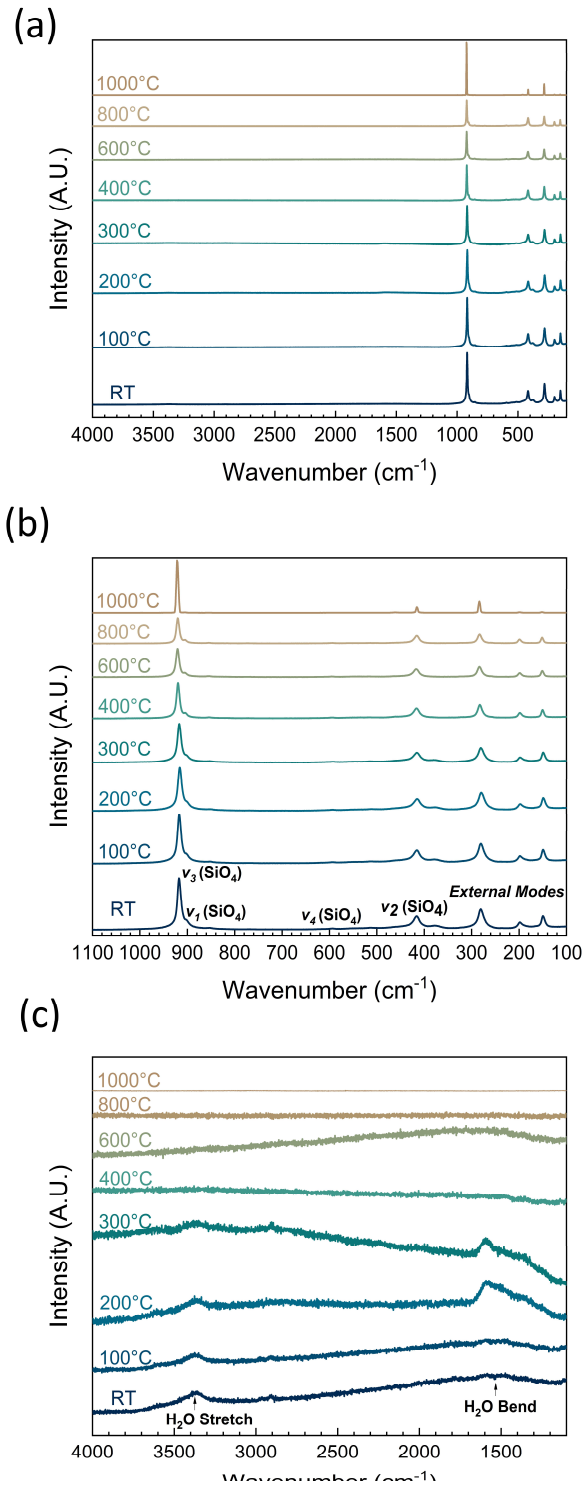

Figure 9. *In situ* high temperature Raman spectroscopy of stetindite for temperatures ranging from room temperature to 1000°C in the regions **(a)** 4000-100cm^{-1}, **(b)** 1100-100cm^{-1} and **(c)** 4000-1000cm^{-1}. Arrows and labels indicate what the various vibrational bands are attributed. v_1, v_2, v_3, v_4 are the 4 normal internal modes of vibration.

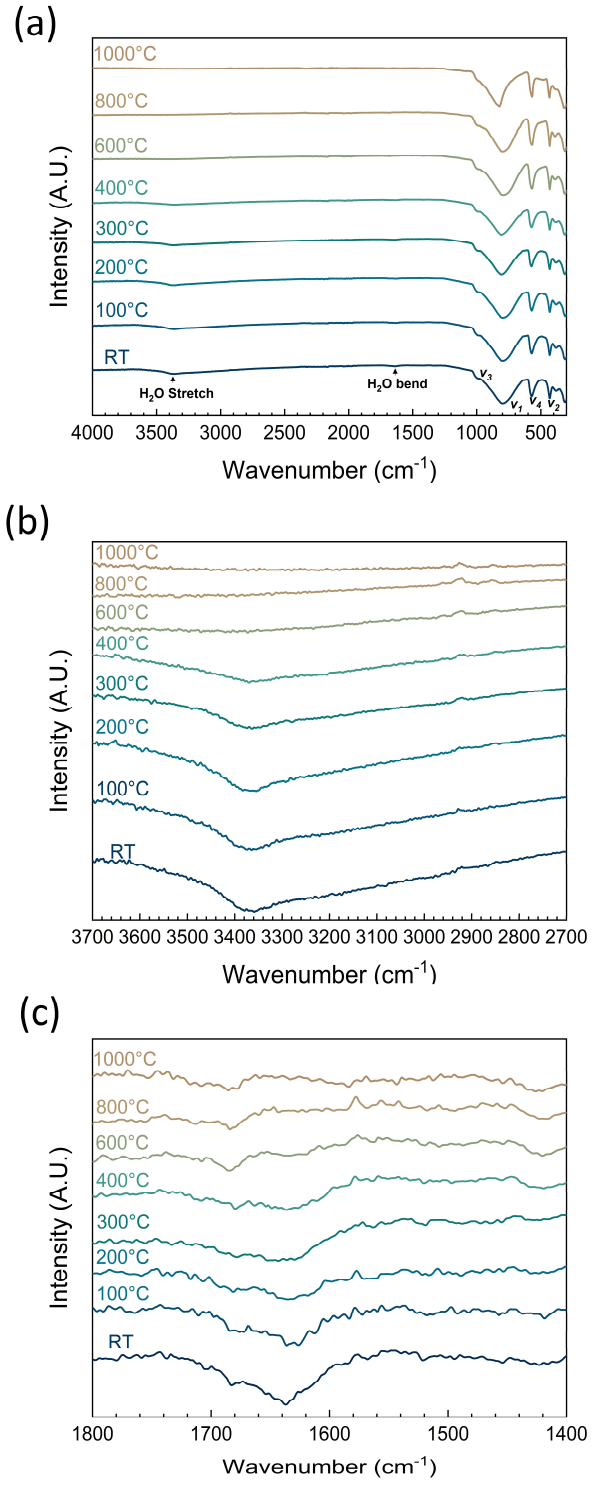

Figure 10. FTIR performed on pristine and calcinated stetindite for temperatures ranging from room temperature to 1000°C in the regions **(a)** 4000-300cm^{-1}, **(b)** 3700-2700cm^{-1} and **(c)** 1800-1400cm^{-1}. Arrows and labels indicate what the various vibrational bands are attributed. v_1, v_2, v_3, v_4 are the 4 normal internal modes of vibration.

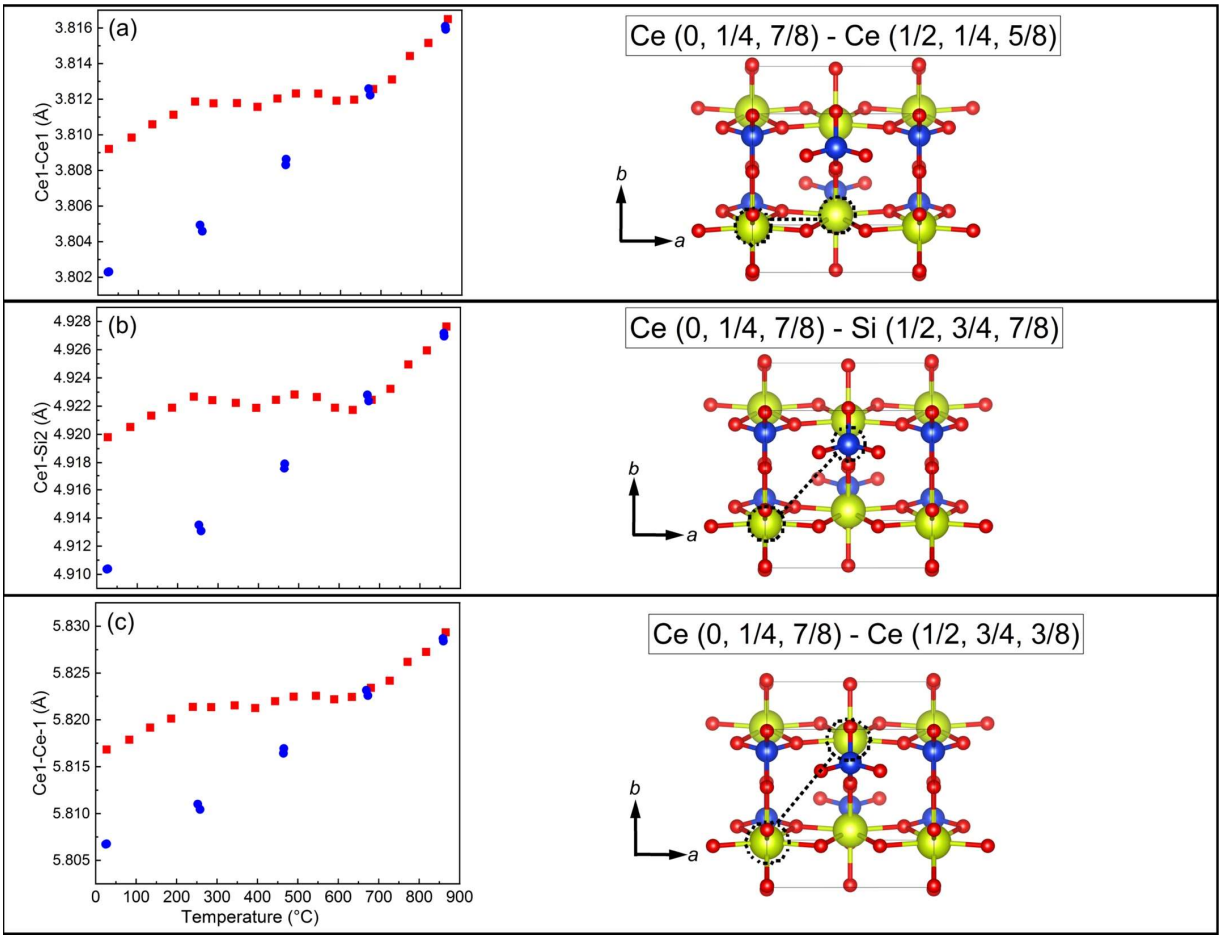

Figure 11. Variation in the measured bond lengths as a function of temperature of the constituting elements which define the dimensions **(a)** height/width, **(b)** diagonal cross-section, and **(c)** depth to the [001] channels of $CeSiO_4$.

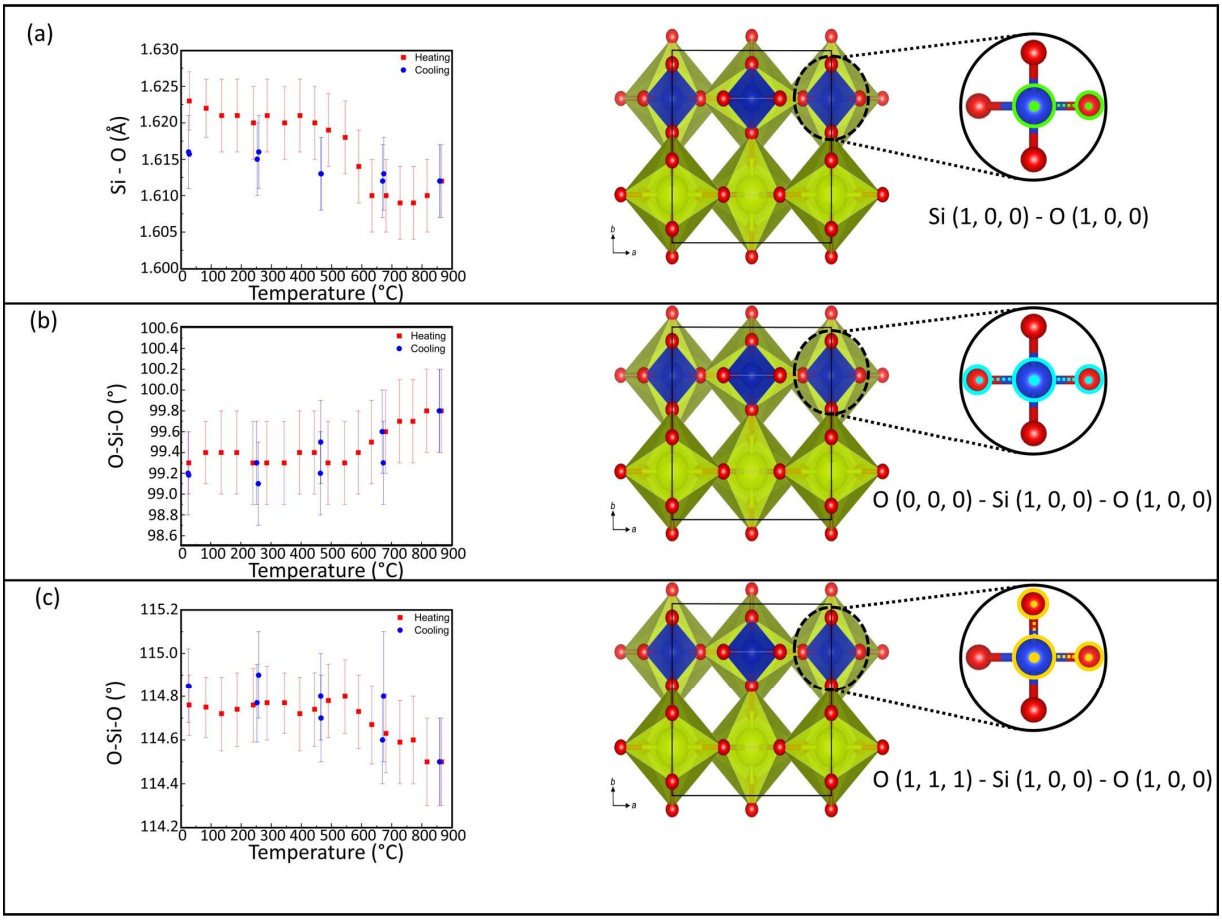

Figure 12. Variation in the measured **(a)** Si-O bond lengths and **(b), (c)** angles of the O-Si-O bonds as a function of temperature for $CeSiO_4$.

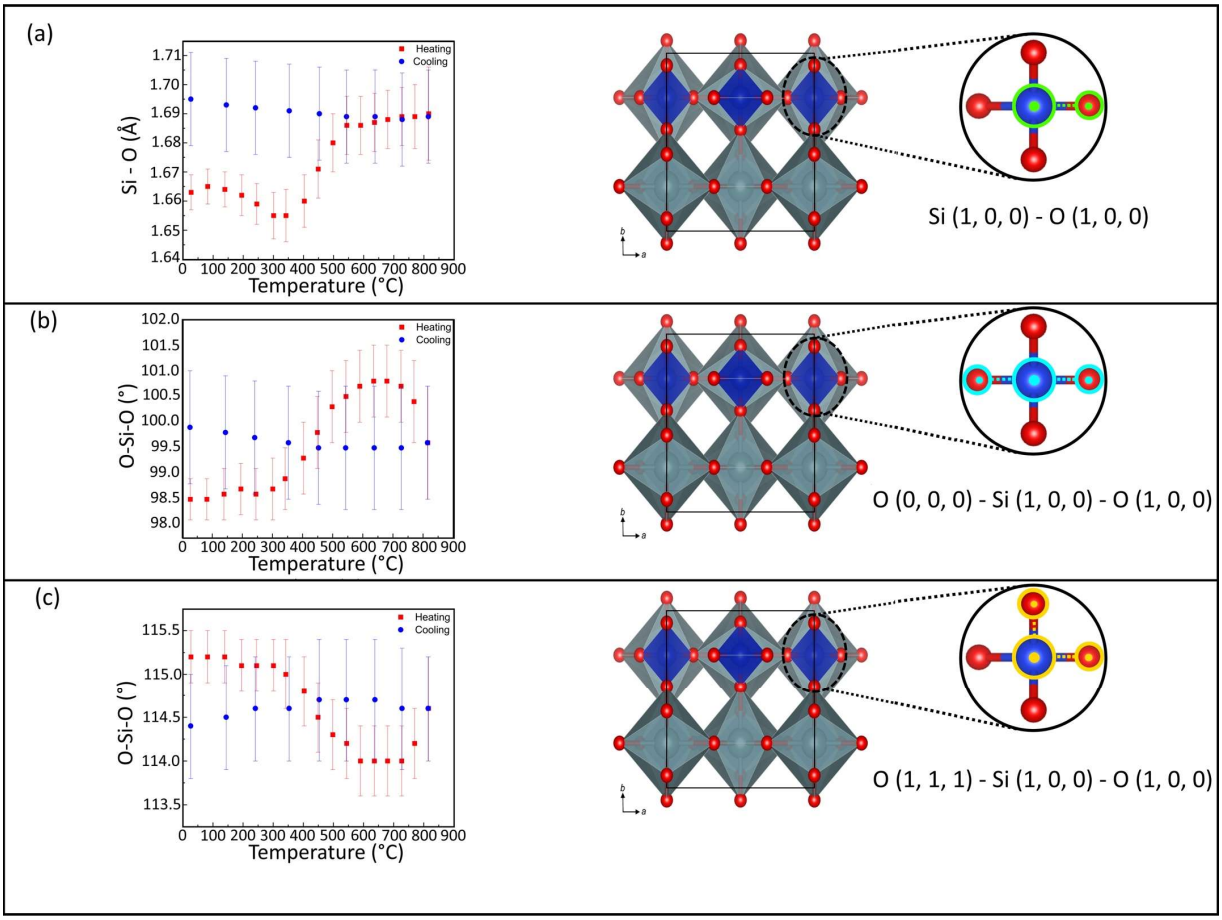

Figure 13. Variation in the measured **(a)** Si-O bond lengths and **(b), (c)** angles of the O-Si-O bonds as a function of temperature for $USiO_4$.

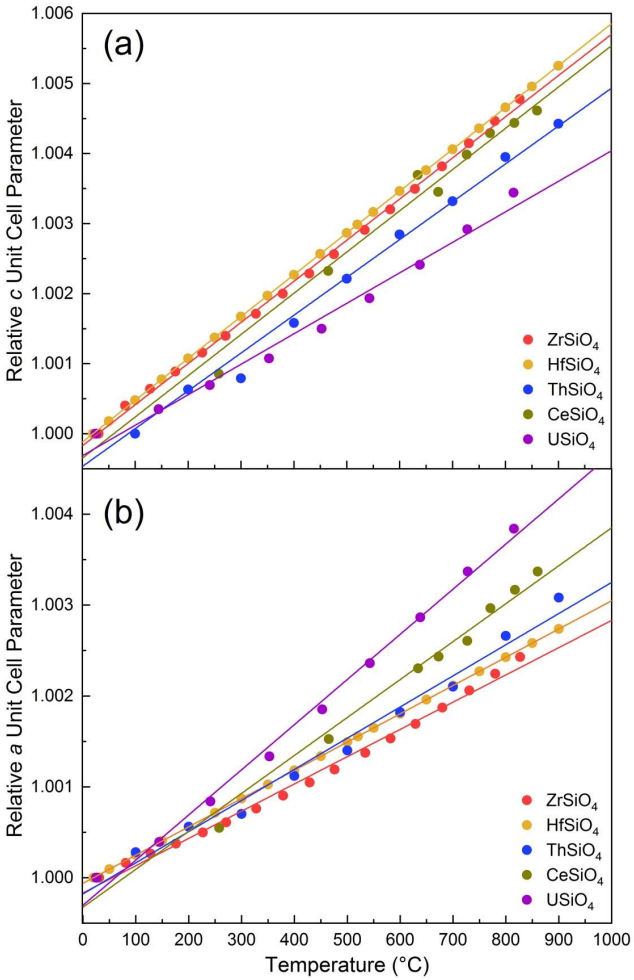

Figure 14. Comparison of the thermal expansion obtained for unit-cell parameters **(a)** *a* and **(b)** *c* for several anhydrous $MSiO_4$ compounds (data from this study for M = Ce, U and data from the literatures for M = Zr, Hf, Th).[89,111,112]

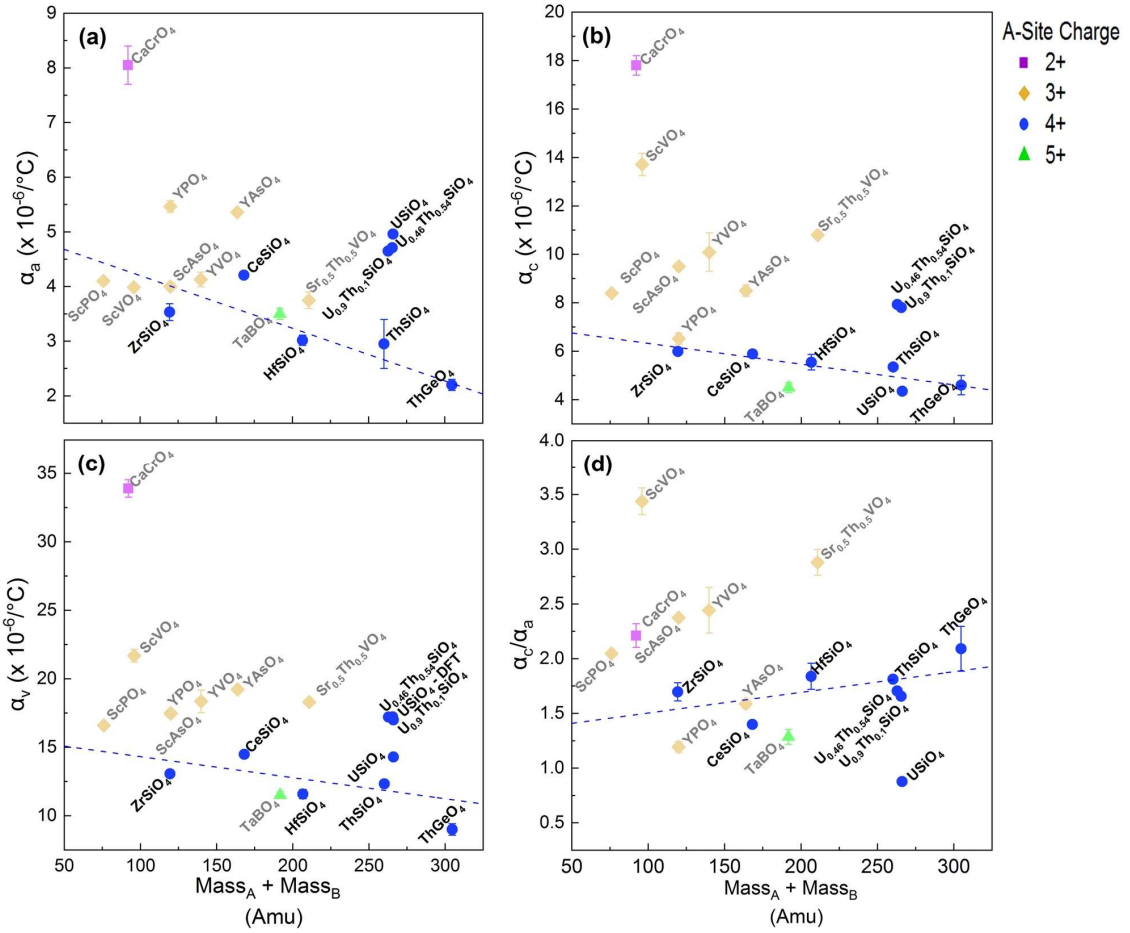

Figure 15. Comparison of the coefficients of thermal expansion of various zircon-type materials as a function of sum of the mass of the A and B site cations. The dashed blue trend line describes only the $A^{4+}B^{4+}O_4$ zircon structure-types. A detailed description of the source of the data points is provided in the SI (Tables S6, S7, and S8)[89,111–115].

ASSOCIATED CONTENT

The Supporting Information is available: PXRD, CTE analyses, FTIR, Raman, and additional information about hydrated and hydroxylated phases.

References

(1) Bell, D. R.; Rossman, G. R. Water in Earth's Mantle: The Role of Nominally Anhydrous Minerals. *Science* (80-.). **1992**, 255, 1391–1397.

(2) Winter, J. D. Principles of Igneous and Metamorphic Petrology, 2nd ed.; *Pearson*, **2013**.

(3) Shelyug, A.; Mesbah, A.; Szenknect, S.; Clavier, N.; Dacheux, N.; Navrotsky, A. Thermodynamics and Stability of Rhabdophanes, Hydrated Rare Earth Phosphates $REPO_4 \cdot nH_2O$. *Front. Chem.* **2018**, 6 (December), 1–11. https://doi.org/10.3389/fchem.2018.00604.

(4) Kubatko, K. A. H.; Helean, K. B.; Navrotsky, A.; Burns, P. C. Stability of Peroxide-Containing Uranyl Minerals. *Science* **2003**, 302 (5648), 1191–1193. https://doi.org/10.1126/science.1090259.

(5) Guo, X.; Ushakov, S. V.; Labs, S.; Curtius, H.; Bosbach, D.; Navrotsky, A. Energetics of Metastudtite and Implications for Nuclear Waste Alteration. *Proc. Natl. Acad. Sci. U. S. A.* **2014**, 111 (50), 17737–17742. https://doi.org/10.1073/pnas.1421144111.

(6) Guo, X.; Wu, D.; Xu, H.; Burns, P. C.; Navrotsky, A. Thermodynamic Studies of Studtite Thermal Decomposition Pathways via Amorphous Intermediates UO_3, U_2O_7, and UO_4. *J. Nucl. Mater.* **2016**, 478, 158–163. https://doi.org/10.1016/j.jnucmat.2016.06.014.

(7) Xu, H.; Guo, X.; Bai, J. Thermal Behavior of Polyhalite: A High-Temperature Synchrotron XRD Study. *Phys. Chem. Miner.* **2017**, 44 (2), 125–135. https://doi.org/10.1007/s00269-016-0842-5.

(8) Guo, X.; Xu, H. Enthalpies of Formation of Polyhalite: A Mineral Relevant to Salt Repository. *J. Chem. Thermodyn.* **2017**, 114, 44–47. https://doi.org/10.1016/j.jct.2017.05.031.

(9) Mesbah, A.; Clavier, N.; Elkaim, E.; Gausse, C.; Kacem, I. Ben; Szenknect, S.; Dacheux, N. Monoclinic Form of the Rhabdophane Compounds: $REEPO_4 \cdot 0.667H_2O$. *Cryst. Growth Des.* **2014**, 14 (10), 5090–5098. https://doi.org/10.1021/cg500707b.

(10) Mesbah, A.; Clavier, N.; Elkaim, E.; Szenknect, S.; Dacheux, N. In Pursuit of the Rhabdophane Crystal Structure: From the Hydrated Monoclinic $LnPO_4 \cdot 0.667H_2O$ to the Hexagonal $LnPO_4$ (Ln = Nd, Sm, Gd, Eu and Dy). *J. Solid State Chem.* **2017**, 249 (February), 221–227. https://doi.org/10.1016/j.jssc.2017.03.004.

(11) Caruba, R.; Baumer, A.; Ganteaume, M.; Iacconi, P. An Experimental Study of Hydroxyl Groups and Water in Synthetic and Natural Zircons: A Model of the Metamict State. *Am. Mineral.* **1985**, 70 (11–12), 1224–1231.

(12) Hawthorne, F. C. The Role of OH and H_2O in Oxide and Oxysalt Minerals. *Zeitschrift fur Krist. - New Cryst. Struct.* **1992**, 201 (3–4), 183–206. https://doi.org/10.1524/zkri.1992.201.3-4.183.

(13) Finch, R. J.; Hanchar, J. M. Structure and Chemistry of Zircon and Zircon-Group Minerals. *Rev. Mineral. Geochemistry* **2003**, 53 (1), 1–26.

(14) Mumpton, F. A.; Roy, R. Hydrothermal Stability Studies of the Zircon-Thorite Group. *Geochim. Cosmochim. Acta* **1961**, 21 (3–4), 217–238. https://doi.org/10.1016/s0016-7037(61)80056-2.

(15) Frondel, C. Systematic Mineralogy of Uranium and Thorium; **1958**; Vol. 1064. https://doi.org/10.3133/b1064.

(16) Pellas, P. Sur La Formation de l'état Métamicte Dans Le Zircon. *Bull. la Société française Minéralogie Cristallogr.* **1954**, 77 (1), 447–460. https://doi.org/10.3406/bulmi.1954.4899.

(17) Clavier, N.; Szenknect, S.; Costin, D. T.; Mesbah, A.; Poinssot, C.; Dacheux, N. From Thorite to Coffinite: A Spectroscopic Study of $Th_{1-X}U_xSiO_4$ Solid Solutions. *Spectrochim. Acta - Part A Mol. Biomol. Spectrosc.* **2014**, 118, 302–307. https://doi.org/10.1016/j.saa.2013.08.093.

(18) Speer, J. A.; Cooper, B. J. Crystal Structure of Synthetic Hafnon, $HfSiO_4$, Comparison with Zircon and the Actinide Orthosilicates. *Am. Mineral.* **1982**, 67 (7–8), 804–808.

(19) Janeczek, J.; Ewing, R. C. Coffinitization - A Mechanism for the Alteration of UO_2 under Reducing Conditions. *Mater. Res. Soc. Symp. Proc.* **1992**, 257. https://doi.org/10.1017/CBO9781107415324.004.

(20) Finch, R.; Murakami, T. Systematics and Paragenesis of Uranium Minerals. In Uranium: Mineralogy, Geochemistry, and the Environment; Burns, P. C., Finch, R. J., Eds.; **1999**; pp 91–179. https://doi.org/10.1515/9781501509193-008.

(21) Janeczek, J. Composition and Origin of Coffinite from Jachymov, Czechoslovakia. *Neues Jahrb. für Mineral. Monatshefte* **1991**, 9, 385–395.

(22) Guo, X.; Szenknect, S.; Mesbah, A.; Labs, S.; Clavier, N.; Poinssot, C.; Ushakov, S. V.; Curtius, H.; Bosbach, D.; Ewing, R. C.; Burns, P.C.; Dacheux, N.; Navrotsky, A. Thermodynamics of Formation of Coffinite, $USiO_4$. *Proc. Natl. Acad. Sci.* **2015**, 112 (21), 6551–6555. https://doi.org/10.1073/pnas.1507441112.

(23) Strzelecki, A. C.; Bourgeois, C.; Kriegsman, K. W.; Estevenon, P.; Wei, N.; Szenknect, S.; Mesbah, A.; Wu, D.; Ewing, R. C.; Dacheux, N.; Guo, X. Thermodynamics of $CeSiO_4$: Implications for Actinide Orthosilicates. *Inorg. Chem.* **2020**, 59 (18), 13174–13183. https://doi.org/10.1021/acs.inorgchem.0c01476.

(24) Guo, X.; Szenknect, S.; Mesbah, A.; Clavier, N.; Poinssot, C.; Wu, D.; Xu, H.; Dacheux, N.; Ewing, R. C.; Navrotsky, A. Energetics of a Uranothorite ($Th_{1-X}U_xSiO_4$) Solid Solution. *Chem. Mater.* **2016**, 28 (19), 7117–7124. https://doi.org/10.1021/acs.chemmater.6b03346.

(25) Weber, W. J.; Ewing, R. C.; Vance, E. R.; Gregg, D.; Peuget, S.; Wiss, T. Plutonium in Waste Forms. In Plutonium Handbook; Clark, D. L., Geeson, D. A., Hanrahan Jr., R. J., Eds.; American Nuclear Society, **2019**; pp 2349–2422.

(26) Ewing, R. C.; Weber, W. J. Actinide Waste Forms and Radiation Effects. In The Chemistry of the Actinide and Transactinide Elements; Morss, L. R., Edelstein, N. M., Fuger, J., Eds.; Springer: Dordrecht, **2010**; Vol. 3813, pp 3813–3887. https://doi.org/10.1007/978-94-007-0211-0_35.

(27) Weber, W. J.; Ewing, R. C. Chapter 10: Ceramic Waste Forms for Uranium and Transuranium Elements. In Uranium: Cradle to Grave; Burns, P. C., Sigmon, G. E., Eds.; Mineralogical Association of Canada, **2013**; pp 317–336.

(28) Lutze, W.; Ewing, R. C. Radioactive Waste Forms for the Future; North-Holland Physics Publishing: Amsterdam, **1988**.

(29) Ewing, R. C. The Design and Evaluation of Nuclear-Waste Forms: Clues from Mineralogy. *Can. Mineral*. **2001**, 39 (3), 697–715. https://doi.org/10.2113/gscanmin.39.3.697.

(30) Ferriss, E. D. A.; Ewing, R. C.; Becker, U. Simulation of Thermodynamic Mixing Properties of Actinide-Containing Zircon Solid Solutions. *Am. Mineral.* **2010**, 95 (2–3), 229–241. https://doi.org/10.2138/am.2010.3318.

(31) Ewing, R. C.; Lutze, W.; Weber, W. J. Zircon: A Host-Phase for the Disposal of Weapons Plutonium. *J. Mater. Res.* **1995**, 10 (2), 243–246. https://doi.org/10.1557/JMR.1995.0243.

(32) Weber, W. J.; Ewing, R. C.; Lutze, W. Performance Assessment of Zircon as a Waste Form for Excess Weapons Plutonium Under Deep Borehole Burial Conditions. *Mater. Res. Soc. Symp. - Proc.* **1996**, 4 12, 25–32. https://doi.org/https://doi.org/10.1557/PROC-412-25.

(33) McMurdie, H. F.; Hall, F. P. Phase Diagrams for Ceramists: Supplement No. 1. J. Am. Ceram. Society **1947**, No. 1, 154–164.

(34) Ewing, R. C.; Weber, W. J.; Clinard, F. W. Radiation Effects in Nuclear Waste Forms for High-Level Radioactive Waste. *Prog. Nucl. Energy* **1995**, 29 (2), 63–127. https://doi.org/10.1016/0149-1970(94)00016-Y.

(35) Nesse, W. D. Introduction to Mineralogy, 2nd ed.; Oxford University Press, **2000**.

(36) White, W. M. Isotope Geochemistry, 1st ed.; John Wiley & Sons, **2015**.

(37) Farnan, I.; Cho, H.; Weber, W. J. Quantification of Actinide α-Radiation Damage in Minerals and Ceramics. *Nature* **2007**, 445 (7124), 190–193. https://doi.org/10.1038/nature05425.

(38) Burns, P. C.; Ewing, R. C.; Navrotsky, A. Nuclear Fuel in a Reactor Accident. *Science* (80-.). **2012**, 335 (6073), 1184–1188. https://doi.org/10.1126/science.1211285.

(39) Ewing, R. C. Long-Term Storage of Spent Nuclear Fuel. *Nat. Mater.* **2015**, 14 (3), 252–257. https://doi.org/10.1038/nmat4226.

(40) Olds, T. A.; Karcher, S. E.; Kriegsman, K. W.; Guo, X.; McCloy, J. S. Oxidation and Anion Lattice Defect Signatures of Hypostoichiometric Lanthanide-Doped UO_2. *J. Nucl. Mater.* **2020**, 530, 151959. https://doi.org/10.1016/j.jnucmat.2019.151959.

(41) Zamoryanskaya, M. V.; Burakov, B. E. Feasibility Limits in Using Cerium as a Surrogate for Plutonium Incorporation in Zircon, Zirconia and Pyrochlore. *Mater. Res. Soc. Symp. - Proc.* **2001**, 663, 301–306. https://doi.org/10.1557/proc-663-301.

(42) Putnam, R. L.; Gallegos, U. F.; Ebbinghaus, B. B.; Navrotsky, A.; Helean, K. B.; Ushakov, S. V; Woodfield, B. F.; Boerio-Goates, J.; Williamson, M. A. Formation Energetics of Ceramic Phases Related to Surplus Plutonium Disposition; Los Alamos, **2000**.

(43) Putnam, R. L.; Navrotsky, A.; Cordfunke, E. H. P.; Huntelaar, M. E. Thermodynamics of Formation of Two Cerium Aluminum Oxides,$CeAlO_{3(s)}$ and $CeAl_{12}O_{19.918(s)}$, and Cerium Sesquioxide,$Ce_2O_{3(s)}$ At T= 298.15 K. *J. Chem. Thermodyn.* **2000**, 32 (7), 911–921. https://doi.org/10.1006/jcht.2000.0665.

(44) Marra, J. C.; Cozzi, A. D.; Pierce, R. A.; Pareizs, J. M.; Jurgensen, A. R.; Missimer, D. M. Cerium as a Surrogate in the Plutonium Immobilized Form. In Environmental Issues and Waste Management Technologies in the Ceramic and Nuclear Industries; Smith, G. L., Sundaram, S. K., Spearing, D. R., Eds.; American Ceramic Society, **2002**; pp 381–388.

(45) Goel, A.; McCloy, J. S.; Pokorny, R.; Kruger, A. A. Challenges with Vitrification of Hanford High-Level Waste (HLW) to Borosilicate Glass – An Overview. *J. Non-Crystalline Solids X* **2019**, 4 (August), 1–19. https://doi.org/10.1016/j.nocx.2019.100033.

(46) Wegel, S.; Czempinski, V.; Oei, P.-Y.; Wealer, B. Transporting and Storing High-Level Nuclear Waste in the U.S.-Insights from a Mathematical Model. *Appl. Sci.* **2019**, 9 (12). https://doi.org/10.3390/app9122437.

(47) Weber, W. J.; Navrotsky, A.; Stefanovsky, S.; Vance, E. R.; Vernaz, E. Materials Science of High-Level Immobilization. *MRS Bull.* **2009**, 34 (January 2009). https://doi.org/https://doi.org/10.1557/mrs2009.12.

(48) Buscheck, T. A.; Glascoe, L. G.; Lee, K. H.; Gansemer, J.; Sun, Y.; Mansoor, K. Validation of the Multiscale Thermohydrologic Model Used for Analysis of a Proposed Repository at Yucca Mountain. *J. Contam. Hydrol.* **2003**, 62–63, 421–440. https://doi.org/10.1016/S0169-7722(02)00157-2.

(49) Haukwa, C. B.; Wu, Y. S.; Bodvarsson, G. S. Modeling Thermal-Hydrological Response of the Unsaturated Zone at Yucca Mountain, Nevada, to Thermal Load at a Potential Repository. *J. Contam. Hydrol.* **2003**, 62–63, 529–552. https://doi.org/10.1016/S0169-7722(02)00188-2.

(50) Löfman, J. Simulation of Hydraulic Disturbances Caused by the Decay Heat of the Repository in Olkiluoto Simulation of Hydraulic Disturbances Caused by the Decay Heat of the Repository in Olkiluoto; OLKILUOTO, **2005**.

(51) Zhou, W.; Apted, M. J.; Kessler, J. H. The Thermal-Hydrological Impact on Increased Spent-Fuel Storage Capacity in Yucca Mountain Repository. *Nucl. Technol*. **2010**, 170 (2), 336–352. https://doi.org/10.13182/NT10-A9487.

(52) Blanco Martín, L.; Rutqvist, J.; Birkholzer, J. T. Long-Term Modeling of the Thermal-Hydraulic-Mechanical Response of a Generic Salt Repository for Heat-Generating Nuclear Waste. *Eng. Geol.* **2015**, 193, 198–211. https://doi.org/10.1016/j.enggeo.2015.04.014.

(53) Reynolds, H. S. Synthesis, Characterisation and Dissolution Studies of the Uranium Mineral Coffinite, Royal Melbourne Institute of Technology University, **2013**.

(54) Fuchs, L. H.; Gebert, E. X-Ray Studies of Synthetic Coffinite, Thorite, and Uranothorites. *Am. Mineral.* **1958**, 43 (2), 243–248.

(55) Speer, J. A. The Actinide Orthosilicates. In Reviews in Mineralogy and Geochemistry; **1982**; Vol. 5, pp 113–136.

(56) Speer, J. A. Zircon. In Reviews in Mineralogy and Geochemistry; **1982**; Vol. 5, pp 66–112.

(57) Stieff, L. R.; Stern, T. W.; Sheerwood, A. M. Coffinite, A Uranous Silicate with Hydroxyl Substitution: A New Mineral. *Am. Mineral.* **1956**, 41, 675–688.

(58) Förster, H. J. Composition and Origin of Intermediate Solid Solutions in the System Thorite-Xenotime-Zircon-Coffinite. *Lithos* **2006**, 88 (1–4), 35–55. https://doi.org/10.1016/j.lithos.2005.08.003.

(59) Zhang, M.; Salje, E. K. H.; Ewing, R. C. Infrared Spectra of Si-O Overtones, Hydrous Species, and U Ions in Metamict Zircon: Radiation Damage and Recrystallization. *J. Phys. Condens. Matter* **2002**, 14 (12), 3333–3352. https://doi.org/10.1088/0953-8984/14/12/319.

(60) Zhang, F. X.; Pointeau, V.; Shuller, L. C.; Reaman, D. M.; Lang, M.; Liu, Z.; Hu, J.; Panero, W. R.; Becker, U.; Poinssot, C.; Ewing, R.C. Structural Transitions and Electron Transfer in Coffinite, $USiO_4$, at High Pressure. *Am. Mineral.* **2009**, 94 (7), 916–920. https://doi.org/10.2138/am.2009.3111.

(61) Deditius, A. P.; Utsunomiya, S.; Ewing, R. C. The Chemical Stability of Coffinite, $USiO_4 \cdot nH_2O$; $0 < n < 2$, Associated with Organic Matter: A Case Study from Grants Uranium Region, New Mexico, USA. *Chem. Geol.* **2008**, 251 (1–4), 33–49. https://doi.org/10.1016/j.chemgeo.2008.02.009.

(62) Nasdala, L.; Beran, A.; Libowitzky, E.; Wolf, D. The Incorporation of Hydroxyl Groups and Molecular Water in Natural Zircon ($ZrSiO_4$). *Am. J. Sci.* **2001**, 301 (10), 831–857. https://doi.org/10.2475/ajs.301.10.831.

(63) Fuchs, L. H.; Hoekstra, H. R. The Preparation and Properties of Uranium (IV) Silicate. *Am. Mineral.* 1959, 44, 1057–1063.

(64) Hoekstra, H. R.; Fuchs, L. H. Synthesis of Coffinite - $USiO_4$. *Science* (80-.). **1956**, 123 (3186), 105.

(65) Pointeau, V.; Deditius, A. P.; Miserque, F.; Renock, D.; Becker, U.; Zhang, J.; Clavier, N.; Dacheux, N.; Poinssot, C.; Ewing, R. C. Synthesis and Characterization of Coffinite. *J. Nucl. Mater.* **2009**, 393 (3), 449–458. https://doi.org/10.1016/j.jnucmat.2009.06.030.

(66) Estevenon, P.; Kaczmarek, T.; Vadot, F.; Dumas, T.; Solari, P. L.; Welcomme, E.; Szenknect, S.; Mesbah, A.; Moisy, P.; Poinssot, C.; Dacheux, N. Formation of $CeSiO_4$ from Cerium (III) Silicate Precursors. *Dalt. Trans.* **2019**, 48, 10455–10463. https://doi.org/10.1039/c9dt01990a.

(67) Mesbah, A.; Szenknect, S.; Clavier, N.; Lozano-Rodriguez, J.; Poinssot, C.; Den Auwer, C.; Ewing, R. C.; Dacheux, N. Coffinite, $USiO_4$, Is Abundant in Nature: So Why Is It so Difficult to Synthesize? *Inorg. Chem.* **2015**, 54 (14), 6687–6696. https://doi.org/10.1021/ic502808n.

(68) Dacheux, N.; Brandel, V.; Genet, M. Synthesis and Properties of Uranium Chloride Phosphate Tetrahydrate: $UClPO_4 \cdot 4H_2O$. New J. Chem. 1995, 19 (10), 1029–1036.

(69) Dacheux, N.; Brandel, V.; Genet, M. Synthese et Caracterisation de l'orthophosphate d'uranium a Valence Mixte: $U(UO_2)(PO_4)_2$. *New J. Chem.* **1995**, 19 (1), 15–26.

(70) Dacheux, N.; Brandel, V.; Genet, M.; Bak, K.; Berthier, C. Solid Solutions of Uranium and Thorium Phosphates: Synthesis, Characterization and X-ray Photoelectron Spectroscopy. *New J. Chem.* **1996**, 20 (3), 301–310.

(71) Clavier, N.; Szenknect, S.; Costin, D. T.; Mesbah, A.; Ravaux, J.; Poinssot, C.; Dacheux, N. Purification of Uranothorite Solid Solutions from Polyphase Systems. *J. Nucl. Mater.* **2013**, 441 (1–3), 73–83. https://doi.org/10.1016/j.jnucmat.2013.05.032.

(72) Prescher, C.; Prakapenka, V. B. DIOPTAS: A Program for Reduction of Two-Dimensional X-ray Diffraction Data and Data Exploration. *High Press. Res.* **2015**, 35 (3), 223–230. https://doi.org/10.1080/08957959.2015.1059835.

(73) Toby, B. H.; Von Dreele, R. B. GSAS-II: The Genesis of a Modern Open-Source All Purpose Crystallography Software Package. *J. Appl. Crystallogr.* **2013**, 46 (2), 544–549. https://doi.org/10.1107/S0021889813003531.

(74) Xu, H.; Chavez, M. E.; Mitchell, J. N.; Garino, T. J.; Schwarz, H. L.; Rodriguez, M. A.; Rademacher, D. X.; Nenoff, T. M. Crystal Structure and Thermodynamic Stability of Ba/Ti-Substituted Pollucites for Radioactive Cs/Ba Immobilization. *J. Am. Ceram. Soc.* **2015**, 98 (8), 2634–2640. https://doi.org/10.1111/jace.13608.

(75) Guo, X.; Lü, X.; White, J. T.; Benmore, C. J.; Nelson, A. T.; Roback, R. C.; Xu, H. Bulk Moduli and High Pressure Crystal Structure of U_3Si_2. *J. Nucl. Mater.* **2019**, 523, 135–142. https://doi.org/10.1016/j.jnucmat.2019.06.006.

(76) Strzelecki, A. C.; Kriegsman, K. W.; Estevenon, P.; Goncharov, V.; Bai, J.; Szenknect, S.; Mesbah, A.; Wu, D.; McCloy, J. S.; Dacheux, N.; Guo, X. High-Temperature Thermodynamics of Cerium Silicates, A-$Ce_2Si_2O_7$ and $Ce_{4.67}(SiO_4)_3O$. *ACS Earth Sp. Chem.* **2020**, 4 (11), 2129–2143. https://doi.org/10.1021/acsearthspacechem.0c0023.

(77) Lü, X.; Stoumpos, C. C.; Hu, Q.; Ma, X.; Zhang, D.; Guo, S.; Hoffman J.; Bu, K; Guo, X.; Wang, Y.; Ji, C.; Chen, H.; Xu, H.; Jia, Q.; Yang, W.; Kanatzidis, M. G.; Mao, H. K. Regulating Off-centering Distortion Maximizes Photoluminescence in Halide Perovskites. *Natl. Sci. Rev.* **2020** (*in press.*) https://doi.org/10.1093/nsr/nwaa288.

(78) Frontera, C.; Rodríguez-Carvajal, J. FullProf as a New Tool for Flipping Ratio Analysis. *Phys. B Condens. Matter* **2003**, 335 (1–4), 219–222. https://doi.org/10.1016/S0921-4526(03)00241-2.

(79) Podor, R.; Nkou Bouala, G. I.; Ravaux, J.; Lautru, J.; Clavier, N. Working with the ESEM at High Temperature. *Mater. Charact.* **2019**, *151*, 15–26.(80)

(80) Frondel, C.; Collette, R. L. Hydrothermal Synthesis of Zircon, Thorite and Huttonite. *Am. Mineral.* **1957**, *42* (378), 759–765.

(81) Taylor, M.; Ewing, R. C. The Crystal Structures of the $ThSiO_4$ Polymorphs: Huttonite and Thorite. *Acta Crystallogr. Sect. B Struct. Crystallogr. Cryst. Chem.* **1978**, *34* (4), 1074–1079. https://doi.org/10.1107/s0567740878004951.

(82) Mazeina, L.; Ushakov, S. V.; Navrotsky, A.; Boatner, L. A. Formation Enthalpy of ThSiO4 and Enthalpy of the Thorite → Huttonite Phase Transition. *Geochim. Cosmochim. Acta* **2005**, *69* (19), 4675–4683. https://doi.org/10.1016/j.gca.2005.03.053.

(83) Labs, S.; Hennig, C.; Weiss, S.; Curtius, H.; Zänker, H.; Bosbach, D. Synthesis of Coffinite, $USiO_4$, and Structural Investigations of $U_xTh_{(1-x)}SiO_4$ Solid Solutions. *Environ. Sci. Technol.* **2014**, *48* (1), 854–860. https://doi.org/10.1021/es403995b.

(84) Szenknect, S.; Mesbah, A.; Cordara, T.; Clavier, N.; Brau, H. P.; Le Goff, X.; Poinssot, C.; Ewing, R. C.; Dacheux, N. First Experimental Determination of the Solubility Constant of Coffinite. *Geochim. Cosmochim. Acta* **2016**, *181*, 36–53. https://doi.org/10.1016/j.gca.2016.02.010.

(85) Mulak, J. Crystal Field Parameters in USiO4 from Temperature Dependence of Paramagnetic Susceptibility. *J. Solid State Chem.* **1977**, *21* (2), 117–126. https://doi.org/10.1016/0022-

4596(77)90151-7.

(86) Bauer, J. D.; Labs, S.; Weiss, S.; Bayarjargal, L.; Morgenroth, W.; Milman, V.; Perlov, A.; Curtius, H.; Bosbach, D.; Zänker, H.; Winkler, B. High-Pressure Phase Transition of Coffinite, $USiO_4$. *J. Phys. Chem. C* **2014**, *118* (43), 25141–25149. https://doi.org/10.1021/jp506368q.

(87) Costin, D. T.; Mesbah, A.; Clavier, N.; Dacheux, N.; Poinssot, C.; Szenknect, S.; Ravaux, J. How to Explain the Difficulties in the Coffinite Synthesis from the Study of Uranothorite? *Inorg. Chem.* **2011**, *50* (21), 11117–11126. https://doi.org/10.1021/ic2016758.

(88) Costin, D. T.; Mesbah, A.; Clavier, N.; Szenknect, S.; Dacheux, N.; Poinssot, C.; Ravaux, J.; Brau, H. P. Preparation and Characterization of Synthetic $Th_{0.5}U_{0.5}SiO_4$ Uranothorite. *Prog. Nucl. Energy* **2012**, *57*, 155–160. https://doi.org/10.1016/j.pnucene.2011.10.004.

(89) Knyazev, A. V.; Komshina, M. E.; Savushkin, I. A. Synthesis and High-Temperature X-Ray Diffraction Study of Thorium Orthosilicate. *Radiochemistry* **2017**, *59* (3), 225–228. https://doi.org/10.1134/S106636221703002X.

(90) Marcial, J.; Zhang, J.; Zhao, X.; Mesbah, A.; Nienhuis, E.; Szenknect, S.; Qi. L.; Lin, J.; Ewing, R. C.; Dacheux, N.; McCloy, J. S.; Guo, X. Origins of Thermodynamic Non-ideality in Coffinite-Thorite Solid Solution. *Npj Mater. Degrad.* **2020**, *Submitted*.

(91) Dawson, P.; Hargreave, M. M.; Wilkinson, G. R. The Vibrational Spectrum of Zircon ($ZrSiO_4$). *J. Phys. C Solid State Phys.* **1971**, *4* (2), 240–256. https://doi.org/10.1088/0022-3719/4/2/014.

(92) Kolesov, B. A.; Geiger, C. A.; Armbruster, T. The Dynamic Properties of Zircon Studied by Single-Crystal X-Ray Diffraction and Raman Spectroscopy. *Eur. J. Mineral.* **2001**, *13* (5), 939–948. https://doi.org/10.1127/0935-1221/2001/0013-0939.

(93) Hoskin, P. W. O.; Rodgers, K. A. Raman Spectral Shift in the Isomorphous $(Zr_{1-X}Hf_x)SiO_4$. *Eur. J. solid state Inorg. Chem.* **1996**, *33* (11), 1111–1121.

(94) Syme, R. W. G.; Lockwood, D. J.; Kerr, H. J. Raman Spectrum of Synthetic Zircon ($ZrSiO_4$) and Raman Spectrum of Synthetic Zircon ($ZrSiO_4$) and Thorite. *Solid State Phys.* **1977**, *10*, 1335–1348.

(95) Estevenon, P.; Welcomme, E.; Szenknect, S.; Mesbah, A.; Moisy, P.; Poinssot, C.; Dacheux, N. Preparation of $CeSiO_4$ from Aqueous Precursors under Soft Hydrothermal Conditions . *Dalt. Trans.* **2019**, *48* (22), 7551–7559. https://doi.org/10.1039/c9dt01258c.

(96) Libowitzky, E.; Beran, A. IR Spectroscopic Characterisation of Hydrous Species in Minerals. In *Spectroscopic methods in mineralogy*; Beran, A., Libowitzky, E., Eds.; Mineralogical Society of Great Britain and Ireland, 2004; pp 227–279.

(97) Woodhead, J. A.; Rossman, G. R.; Thomas, A. P. Hydrous Species in Zircon. *Am. Mineral.* **1991**, *76* (9–10), 1533–1546.

(98) Gillet, P.; Le Cheach, A. High-Temperature Raman Spectroscopy of SiO_2 and GeO_2 Polymorphs: Anharmonicity and Thermodynamic Properties at High-Temperatures. *J. Geophys. Res.* **1990**, *95* (90), 21635–21655.

(99) Knittle, E.; Williams, Q. High-Pressure Raman Spectroscopy of $ZrSiO_4$: Observation of the Zircon to Scheelite Transition at 300 K. *Am. Mineral.* **1993**, *78* (3–4), 245–252.

(100) Hansley, P. L.; Fitzpatrick, J. J. Compositional and Crystallographic Data on REE-Bearing Coffinite from the Grants Uranium Region, Northwestern New Mexico. *Am. Mineral.* **1989**, *74*

(7), 263–270.

(101) Darnley, A. G.; English, T. H.; Sprake, O.; Preece, E. R.; Avery, D. Ages of Uraninite and Coffinite from South-West England. *Mineral. Mag. J. Mineral. Soc.* **1965**, *34* (268), 159–176. https://doi.org/10.1180/minmag.1965.034.268.13.

(102) Estevenon, P.; Welcomme, E.; Szenknect, S.; Mesbah, A.; Moisy, P.; Poinssot, C.; Dacheux, N. Multiparametric Study of the Synthesis of ThSiO 4 under Hydrothermal Conditions. *Inorg. Chem.* **2018**, *57* (15), 9393–9402. https://doi.org/10.1021/acs.inorgchem.8b01390.

(103) Estevenon, P.; Kaczmarek, T.; Rafiuddin, M. R.; Welcomme, E.; Szenknect, S.; Mesbah, A.; Moisy, P.; Poinssot, C.; Dacheux, N. Soft Hydrothermal Synthesis of Hafnon, $HfSiO_4$. *Cryst. Growth Des.* **2020**. https://doi.org/10.1021/acs.cgd.9b01546.

(104) Navrotsky, A.; Ushakov, S. V. *Materials Fundamentals of Gate Dielectrics*; 2005. https://doi.org/10.1007/1-4020-3078-9.

(105) Troost, L.; Ouvrard, L. S. Les Silicates de Thorine. *Comptes rendus l'Académie des Sci.* **1887**, *105*, 255−258.

(106) Fuchs, L. H. Formation and Properties Of synthetic Thorite Crystals. *Am. J. Sci.* **1958**, *43*, 367−368.

(107) Vance, E. R. Thermal Crystallization of $CaTiSiO_5$, $ZrSiO_4$ and $ThSiO_4$ Gels. *Mater. Res. Bull.* **1986**, *21* (3), 321–329. https://doi.org/10.1016/0025-5408(86)90189-3.

(108) Keller, V. C. Untersuchungen Über Die Germanate Und Silikate Des Typs ABO4 Der Vierwertigen Elemente Thorium Bis Americium. *Nukleonik* **1963**, No. 5, 41–48.

(109) Subramani, T.; Rafiuddin, M. R.; Shelyug, A.; Ushakov, S. V.; Mesbah, A.; Clavier, N.; Qin, D.; Szenknect, S.; Elkaim, E.; Dacheux, N.; Navrotsky, A. Synthesis, Crystal Structure and Enthalpies of Formation of Churchite-Type $REPO_4 \cdot 2H_2O$ (RE = Gd to Lu) Materials. *Cryst. Growth Des.* **2019**, acs.cgd.9b00524. https://doi.org/10.1021/acs.cgd.9b00524.

(110) Qin, D.; Mesbah, A.; Clavier, N.; Szenknect, S.; Dacheux, N. From Th-Rhabdophane to Monazite-Cheralite Solid Solutions: Thermal Behavior of $Nd_{1-2x}Th_xCa_xPO_4 \cdot nH_2O$ (x = 0–0.15). *Cryst. Growth Des.* **2019**, acs.cgd.9b00028. https://doi.org/10.1021/acs.cgd.9b00028.

(111) Mursic, Z.; Vogt, T.; Frey, F. High-temperature Neutron Powder Diffraction Study of $ZrSiO_4$ up to 1900 K. *Acta Crystallogr. Sect. B* **1992**, *48* (5), 584–590. https://doi.org/10.1107/S0108768192002982.

(112) Ding, Z.; Ridley, M.; Deijkers, J.; Liu, N.; Hoque, M. S. Bin; Gaskins, J.; Zebarjadi, M.; Hopkins, P.; Wadley, H.; Opila, E.; Esfarjani, K. The Physical and Mechanical Properties of Hafnium Orthosilicate: Experiments and First-Principles Calculations. *Preprint* **2020**.

(113) Bayer, G. Thermal Expansion of ABO4-Compounds with Zircon- and Scheelite Structures. *J. Less-Common Met.* **1972**, *26* (2), 255–262. https://doi.org/10.1016/0022-5088(72)90045-8.

(114) Subbarao, E. C.; Agrawal, D. K.; McKinstry, H. A.; Sallese, C. W.; Roy, R. Thermal Expansion of Compounds of Zircon Structure. *J. Am. Ceram. Soc.* **1990**, *73* (5), 1246–1252. https://doi.org/10.1111/j.1151-2916.1990.tb05187.x.

(115) Varghese, J.; Joseph, T.; Surendran, K. P.; Rajan, T. P. D.; Sebastian, M. T. Hafnium Silicate: A New Microwave Dielectric Ceramic with Low Thermal Expansivity. *Dalt. Trans.* **2015**, *44* (11), 5146–5152. https://doi.org/10.1039/c4dt03367a.

(116) Fleche, J. L. Thermodynamical Functions for Crystals with Large Unit Cells Such as Zircon, Coffinite, Fluorapatite, and Iodoapatite from Ab Initio Calculations. *Phys. Rev. B - Condens. Matter Mater. Phys.* **2002**, *65* (24), 1–10. https://doi.org/10.1103/PhysRevB.65.245116.

(117) Li, H.; Zhou, S.; Zhang, S. The Relationship between the Thermal Expansions and Structures of ABO_4 Oxides. *J. Solid State Chem.* **2007**, *180* (2), 589–595. https://doi.org/10.1016/j.jssc.2006.11.023.

(118) Vitova, T.; Pidchenko, I.; Fellhauer, D.; Bagus, P. S.; Joly, Y.; Pruessmann, T.; Bahl, S.; Gonzalez-Robles, E.; Rothe, J.; Altmaier, M.; Denecke, M.A.; Geckeis, H. The Role of the 5f Valence Orbitals of Early Actinides in Chemical Bonding. *Nat. Commun.* **2017**, *8* (May), 1–9. https://doi.org/10.1038/ncomms16053.

(119) Neidig, M. L.; Clark, D. L.; Martin, R. L. Covalency in F-Element Complexes. *Coord. Chem. Rev.* **2013**, *257* (2), 394–406. https://doi.org/10.1016/j.ccr.2012.04.029.

(120) Su, L.; Wan, L.; Gao, T.; Ao, B. First-Principles Calculations of the Electronic Structure, Chemical Bonding, and Thermodynamic Properties of USiO 4 . *AIP Adv.* **2020**, *10* (7), 075018. https://doi.org/10.1063/5.0018203.

(121) Tobin, J. G.; Yu, S. W.; Booth, C. H.; Tyliszczak, T.; Shuh, D. K.; Van Der Laan, G.; Sokaras, D.; Nordlund, D.; Weng, T. C.; Bagus, P. S. Oxidation and Crystal Field Effects in Uranium. *Phys. Rev. B - Condens. Matter Mater. Phys.* **2015**, *92* (3), 1–12. https://doi.org/10.1103/PhysRevB.92.035111.

(122) Navrotsky, A. Systematic Trends and Prediction of Enthalpies of Formation of Refractory Lanthanide and Actinide Ternary Oxide Phases. *Ceram. Trans.* **2001**, No. 119, 137–146.

(123) Helean, K. B.; Navrotsky, A.; Lumpkin, G. R.; Colella, M.; Lian, J.; Ewing, R. C.; Ebbinghaus, B.; Catalano, J. G. Enthalpies of Formation of U-, Th-, Ce-Brannerite: Implications for Plutonium Immobilization. *J. Nucl. Mater.* **2003**, *320* (3), 231–244. https://doi.org/10.1016/S0022-3115(03)00186-7.

(124) Navrotsky, A. Thermochemical Insights into Refractory Ceramic Materials Based on Oxides with Large Tetravalent Cations. *J. Mater. Chem.* **2005**, *15* (19), 1883–1890. https://doi.org/10.1039/b417143h.

(125) Qi, J.; Guo, X.; Mielewczyk-Gryn, A.; Navrotsky, A. Formation Enthalpies of $LaLnO_3$ (Ln=Ho, Er, Tm and Yb) Interlanthanide Perovskites. *J. Solid State Chem.* **2015**, *227*, 150–154. https://doi.org/10.1016/j.jssc.2015.03.026.

(126) Helean, K. B.; Ushakov, S. V.; Brown, C. E.; Navrotsky, A.; Lian, J.; Ewing, R. C.; Farmer, J. M.; Boatner, L. A. Formation Enthalpies of Rare Earth Titanate Pyrochlores. *J. Solid State Chem.* **2004**, *177* (6), 1858–1866. https://doi.org/10.1016/j.jssc.2004.01.009.

(127) Guo, X.; Tiferet, E.; Qi, L.; Solomon, J. M.; Lanzirotti, A.; Newville, M.; Engelhard, M. H.; Kukkadapu, R. K.; Wu, D.; Ilton, E. S.; Asta, M.; Sutton, S.R.; Xu, H.; Navrotsky, A. U(v) in Metal Uranates: A Combined Experimental and Theoretical Study of $MgUO_4$, $CrUO_4$, and $FeUO_4$. *Dalt. Trans.* **2016**, *45* (11), 4622–4632. https://doi.org/10.1039/c6dt00066e.

(128) Chen, F.; Ewing, R. C.; Clark, S. B. The Gibbs Free Energies and Enthalpies of Formation of U6+ Phases: An Empirical Method of Prediction. *Am. Mineral.* **1999**, *84* (4), 650–664. https://doi.org/10.2138/am-1999-0418.

(129) Sverjensky, D.; Shock, E. L.; Helgeson, H. C. Prediction of the Thermodynamic Properties of Aqueous Metal Complexes to 1000 C and 5 Kb. *Geochim. Cosmochim. Acta* **1997**, *61* (7), 1359–

1412. https://doi.org/10.1016/S0016-7037(97)00009-4.

(130) Anderson, D. L.; Anderson, O. L. The Bulk Modulus-Volume Relationship for Oxides. *J. Geophys. Res.* **1970**, *75* (17), 3494–3500.

(131) Xu, H.; Zhao, Y.; Zhang, J.; Wang, Y.; Hickmott, D. D.; Daemen, L. L.; Hartl, M. A.; Wang, L. Anisotropic Elasticity of Jarosite: A High-P Synchrotron XRD Study. *Am. Mineral.* **2009**, *95* (1), 19–23. https://doi.org/10.2138/am.2010.3280.

(132) Momma, K.; Izumi, F. VESTA 3 for Three-Dimensional Visualization of Crystal, Volumetric and Morphology Data. *J. Appl. Crystallogr.* **2011**, *44* (6), 1272–1276. https://doi.org/10.1107/S0021889811038970.